Nonperturbative renormalization of bilinear operators with dynamical overlap fermions

J. Noaki,[1] T. W. Chiu,[2] H. Fukaya,[3] S. Hashimoto,[1,4] H. Matsufuru,[1] T. Onogi,[5,*] E. Shintani,[5,*] and N. Yamada[1,4]

(JLQCD and TWQCD Collaborations)

[1]*High Energy Accelerator Research Organization (KEK), Tsukuba 305-0801, Japan*
[2]*Physics Department, Center for Quantum Science and Engineering, and Center for Theoretical Sciences, National Taiwan University, Taipei 10617, Taiwan*
[3]*Department of Physics, Nagoya University, Nagoya 464-8602, Japan*
[4]*School of High Energy Accelerator Science, The Graduate University for Advanced Studies (Sokendai), Tsukuba 305-0801, Japan*
[5]*Yukawa Institute for Theoretical Physics, Kyoto University, Kyoto 606-8502, Japan*
(Received 11 August 2009; published 1 February 2010)

Using the nonperturbative renormalization technique, we calculate the renormalization factors for quark bilinear operators made of overlap fermions on the lattice. The background gauge field is generated by the JLQCD and TWQCD Collaborations, including dynamical effects of two or $2+1$ flavors of light quarks on a $16^3 \times 32$ or $16^3 \times 48$ lattice at lattice spacing around 0.1 fm. By reducing the quark mass close to the chiral limit, where the finite volume system enters the so-called ϵ regime, the unwanted effect of spontaneous chiral symmetry breaking on the renormalization factors is suppressed. On the lattices in the conventional p regime, this effect is precisely subtracted by separately calculating the contributions from the chiral condensate.

DOI: 10.1103/PhysRevD.81.034502 PACS numbers: 11.15.Ha, 12.38.Gc

I. INTRODUCTION

For lattice calculations of operator matrix elements including those of the electroweak effective Hamiltonian, the operator matching is a necessary step to absorb the difference of the renormalization scheme from the conventional continuum one, such as the $\overline{\mathrm{MS}}$ scheme. This is necessary for most composite operators except for those protected by some symmetry, e.g. the conserved vector current, since the operators are defined with a given lattice action and are, in general, divergent in the continuum limit. This operator matching can be done perturbatively and has been done often at the one-loop level, which induces a potential source of large systematic error. Given that the strong coupling constant α_s is in the range 0.2–0.3, a typical size of the two-loop correction is 4%–10%. A nonperturbative technique to calculate this operator matching is therefore highly desirable to achieve a precise calculation of physical quantities.

The nonperturbative renormalization (NPR) method uses the RI/MOM scheme [1] in an intermediate step. This scheme is defined for the amputated Green's function in the Landau gauge with an off-shell momentum, which is spacelike. Since the matching between the RI/MOM and the $\overline{\mathrm{MS}}$ schemes is known to two-loop order in many important operators, the method provides a better matching scheme as a whole, though not all the steps are nonperturbative. Moreover, since the perturbative series is, in general, more convergent in the continuum schemes, the remaining uncertainty can be made small, down to a level of a few percent.

Since the method still requires perturbative expansion, the renormalization condition has to be applied in the region where nonperturbative effects are sufficiently small. On the other hand, one has to avoid large discretization effects that may arise when the renormalization scale is too high. Therefore, the renormalization scale μ must satisfy the condition $\Lambda_{\mathrm{QCD}} \ll \mu \ll \pi/a$, where Λ_{QCD} stands for the QCD scale and a is the lattice spacing. This region is often called the NPR window.

The nonperturbative effect may be enhanced when spontaneous chiral symmetry breaking (SCSB) occurs and (almost) massless pions arise [1]. The reason is that the pion-pole contribution in the pseudoscalar channel diverges towards the massless limit and makes it difficult to find the NPR window. With the Wilson-type fermions, the problem is severer because the error starts at $\mathcal{O}(a)$, and thus the possible window is narrower in the high momentum regime. Even with the on-shell $\mathcal{O}(a)$-improved Wilson fermion, the problem remains since the off-shell amplitude is considered in NPR. With the chirally symmetric lattice actions, such as the domain-wall and overlap fermion formulations, the problem becomes more tractable because the $\mathcal{O}(a)$ error is absent even in off-shell amplitudes.

So far, there have been a number of works that calculate the nonperturbative renormalization factors with the RI/MOM scheme for the domain-wall [2,3] and for the quenched overlap fermions [4–6].

In this work, we study the nonperturbative renormalization factors with the RI/MOM scheme for the quark bilinear operators in unquenched QCD with overlap fermi-

*Present address: Department of Physics, Osaka University Toyonaka, Osaka 560-0043, Japan.

ons. Our motivation is twofold. The first is to provide the renormalization factors corresponding to the two-flavor [7] and 2 + 1-flavor [8,9] gauge configurations generated in the large-scale dynamical overlap project by the JLQCD and TWQCD Collaborations, including the quark mass renormalization factor Z_m that has already been used in a series of publications [10–16]. The second is to study the pion-pole contribution appearing in the NPR calculation in detail and demonstrate a method to control the pion-pole effect in a reliable manner.

Since the low-lying eigenmodes of the Dirac operator are expected to dominate the pion-pole contribution, it is possible to trace their effect as a function of quark mass by explicitly constructing the relevant piece from the low-mode eigenvalues. To be explicit, the pion-pole contribution of the form $\langle\bar{q}q\rangle/p^2$ in the operator product expansion contains the chiral condensate $\langle\bar{q}q\rangle$, which is finite in the vacuum of spontaneously broken chiral symmetry. On the lattice of finite volume V, it quickly vanishes as the quark mass becomes smaller than $\sim 1/\Sigma V$, where Σ is the chiral condensate in the infinite volume limit. We identify this term by explicitly comparing the lattice data of the (inverse) quark propagator with the condensate $\langle\bar{q}q\rangle$ constructed from the eigenvalues. Thus, this unnecessary term for NPR can be identified and subtracted. This means that the pion-pole contribution is no longer a problem for the NPR calculation. Clearly, this is possible only when the chiral symmetry is preserved on the lattice. Otherwise, the chiral condensate has a bad cubic divergence even in the massless limit; hence the identification of its physical contribution is not feasible.

This paper is organized as follows. We describe the profile of the gauge configurations used in this work in Sec. II. In Sec. III, we discuss the NPR method and its relation to spontaneous chiral symmetry breaking and present our analysis. Results of the calculation are given in Sec. III D, where we summarize all results of the renormalization factor available from simple bilinear operators, namely, those for the quark mass, the scalar current, the tensor operator, and the quark field. (The vector and axial-vector currents are treated independently.) Our conclusion is given in Sec. IV.

II. GAUGE CONFIGURATIONS

In order to make this paper self-contained, we briefly describe the generation of the gauge configurations used in this work. We refer to [7–9] for more complete description.

We use the overlap fermion formulation [17,18] on the lattice for both sea and valence quarks. The massless overlap-Dirac operator is defined as

$$D_{\rm ov}(0) = m_0(1 + \gamma_5 \cdot {\rm sgn}[H_W(-m_0)]), \tag{2.1}$$

where $H_W(-m_0) \equiv \gamma_5 D_W(-m_0)$ is the Hermitian Wilson-Dirac operator with a large negative mass $-m_0$. The massive operator with a bare mass m is constructed from this as

$$D_{\rm ov}(m) = \left(1 - \frac{m}{2m_0}\right) D_{\rm ov}(0) + m. \tag{2.2}$$

We use the hybrid Monte Carlo (HMC) algorithm [19] to incorporate the fermionic determinant $\det[D_{\rm ov}(m_{\rm sea})]$ (for each flavor) in the path integral.

Since the overlap-Dirac operator contains the sign function, the corresponding determinant changes discontinuously on the border of the global topological charge of the gauge field configuration, which makes the simulation time-consuming. In order to avoid touching the border, where the sign of the lowest eigenvalue of H_W changes, we introduce two extra flavors of heavy Wilson fermions such that they produce a factor

$$\det\left[\frac{H_W^2(-m_0)}{H_W^2(-m_0) + \mu^2}\right] \tag{2.3}$$

in the Boltzmann weight. Associated (twisted-mass) bosons are also introduced with a twisted-mass μ. They play a role to minimize the change of the effective gauge coupling induced by those extra fermions. Throughout this paper, we choose $m_0 = 1.60$ and $\mu = 0.20$ in lattice units. In [20], the Iwasaki gauge action [21] was found to be a good choice for the efficient minimization. As a result, the topological charge Q of the generated gauge configurations is fixed to its initial value [20]. In this work, we choose $Q = 0$. Although the correct sampling of the θ vacuum of QCD is spoiled due to the fixed topology, the difference is suppressed for large four-volume V, and it is indeed possible to reconstruct the θ-vacuum physics from those evaluated by the path integral in a fixed topology [22]. In any case, such finite volume effects are irrelevant for the calculation of the renormalization constants considered in this work, as we mainly use the high momentum regime.

In Table I, we list the parameter set for each gauge ensemble on which we calculate the renormalization factors in this work. We performed two-flavor ($N_f = 2$) and 2 + 1-flavor ($N_f = 2 + 1$) runs. One of the simulations, "NF2ϵ," is in the so-called ϵ regime of chiral perturbation theory, which corresponds to a very small sea quark mass so that the pion's Compton wavelength is longer than the lattice extent. The sea quark mass $m_{\rm sea} = 0.002$ roughly corresponds to 3 MeV in physical units. Other runs at $N_f = 2$, "NF2p," are in the conventional p regime, where we take six values of $m_{\rm sea}$. The 2 + 1-flavor runs are performed at two different values of the strange quark mass, $m_s = 0.080$ ("NF3p-a") and 0.100 ("NF3p-b"), so that we can interpolate (or extrapolate) the data to the physical strange quark mass afterwards. For each m_s, we take five values of sea quark mass corresponding to the up and down quarks m_{ud}.

We employ the Iwasaki gauge action for the gauge part of the lattice formulation. The parameter β in the action controls the lattice spacing a; we determine the value of the

TABLE I. Parameter set for each gauge ensemble NF2ϵ, NF2p, NF3p-a, and NF3p-b. The number of trajectories are common for all sea quark masses in each ensemble.

Ensemble	NF2ϵ	NF2p	NF3p-a	NF3p-b
N_f	2	2	2 + 1	
β	2.35	2.30	2.30	
a^{-1} (GeV)	1.776(38)	1.667(17)	1.833(12)	
Lattice size	$16^3 \times 32$	$16^3 \times 32$	$16^3 \times 48$	
$m_{\rm sea}$ (m_{ud})	0.002	0.015, 0.025, 0.035, 0.050, 0.070, 0.100	0.015, 0.025, 0.035, 0.050, 0.080	0.015, 0.025, 0.035, 0.050, 0.100
m_s	∞	∞	0.080	0.100
m_q	0.002, 0.015, 0.025, 0.035, 0.050, 0.070, 0.100	0.015, 0.025, 0.035, 0.050, 0.070, 0.100	0.015, 0.025, 0.035, 0.050, 0.080	0.015, 0.025, 0.035, 0.050, 0.100
Number of trajectories	2000	10 000	2500	2500
Number of step traj. (NPR)	10	100	10	
Number of step traj. (WTI)	See text	20	5	
Number of low modes	50×2	50×2	80×2	
Number of $p_{\rm latt}$ ($p^2_{\rm latt}$)	1375 (30)	1375 (30)	1875 (53)	
Relevant papers	[10–12]	[13,15,23]	[16]	

lattice spacing from the Sommer scale r_0 by taking $r_0 = 0.49$ fm as an input after extrapolating the lattice data to the chiral limit $m_{\rm sea} = 0$ or $m_{ud} = 0$ at a fixed β. The spatial lattice size is 16^3, and the temporal size is 32 and 48 for the two-flavor and the 2 + 1-flavor runs, respectively.

The valence quark propagator on each ensemble is computed using the multishift solver at various valence quark masses. For each ensemble in the p regime, we take the same set of masses for the valence quarks as that for the sea quarks listed in Table I. For NF2ϵ, we take seven values of the valence quark mass: $m_q = 0.002$, 0.025, 0.015, 0.035, 0.050, 0.070, and 0.100.

On each gauge configuration fixed to the Landau gauge, we compute the quark propagator $S_{\rm ov}(x|x_{\rm src}) \equiv [D_{\rm ov}(m_q)^{-1}]_{x,x_{\rm src}}$, where the location of the source $x_{\rm src}$ is typically fixed at the origin. To calculate the renormalization factors, we work in the (four-dimensional) momentum space,

$$S_{\rm ov}(p_{\rm latt}) = \sum_x e^{-ip_{\rm latt}\cdot x} S_{\rm ov}(x|x_{\rm src}). \tag{2.4}$$

To avoid possible large discretization errors, we restrict the lattice momentum $p_{\rm latt}$ such that none of its elements, $p^\mu_{\rm latt} = 2\pi n_\mu / L_\mu$, exceeds unity. The number of lattice momenta satisfying this condition are listed in Table I. Some of them are degenerate in their magnitude $(p_{\rm latt})^2$; the number of available data points in $(p_{\rm latt})^2$ are also listed in parentheses. On a $16^3 \times 32$ lattice, for instance, we have 1375 different four-momenta from the condition $-2 \le n_i \le 2$ ($i = 1, 2, 3$) and $-5 \le n_4 \le 5$, and there are 30 different values of $(p_{\rm latt})^2$. When analyzing the lattice data, we first average over different four-momenta giving an identical $(p_{\rm latt})^2$. This way, we obtain the maximal number of data points as a function of momentum, with a comparable quality of signal to those obtained by the momentum source method.

III. RI/MOM RENORMALIZATION ON THE LATTICE

A. Renormalization condition and the axial-Ward-Takahashi identity

We consider flavor nonsinglet bilinear operators of the form $\bar{q}\Gamma q'$ with $\Gamma = \gamma_\mu, \gamma_\mu\gamma_5, I, \gamma_5$, and $\gamma_\mu\gamma_\nu$, which we call V, A, S, P, and T, respectively. In the following, we may omit the prime in q' that indicates that the quark flavor is different from q, but the flavor nonsinglet operator is always assumed.

With the exact chiral symmetry of the overlap fermion, these operators are multiplicatively renormalized as

$$(\bar{q}\Gamma q)^R(\mu) = Z_\Gamma(\mu a)(\bar{q}\Gamma q)^0, \tag{3.1}$$

where superscripts R and 0 represent the renormalized and bare operators, respectively. For divergent operators S, P, and T, the renormalized operator may have a dependence on the renormalization scale μ. The multiplicative renormalization factor $Z_\Gamma(\mu a)$ then depends on the scale μ, too. For the vector and axial-vector currents, the renormalization scale dependence is absent because of the current conservation. In the following notation, we may drop the dependence on μ, as it is implicitly assumed. The quark field q is renormalized as $q^R = Z_q^{1/2}(\mu a) q^0$.

In the RI/MOM scheme [1], the renormalization condition is imposed on the amputated Green's function $\Lambda_\Gamma(p) = \frac{1}{12}\,{\rm Tr}[\langle S(p)\rangle^{-1} G_\Gamma(p) \langle S(p)\rangle^{-1}\Gamma]$ to satisfy

$$\Lambda^R_\Gamma(p) = Z_q^{-1}(\mu) Z_\Gamma \Lambda^0_\Gamma(p) = 1 \tag{3.2}$$

at a spacelike off-shell momentum $p^2 = \mu^2$ in the

chiral limit. Here, the Green's function $G_\Gamma(p) = \langle q(p)|\bar{q}\Gamma q'|\bar{q}'(p)\rangle$ is amputated by the vacuum expectation value of the quark propagator $\langle S(p)\rangle$ and projected with an appropriate gamma matrix Γ. (The "Tr" denotes the trace over the color and spinor indices.) The RI/MOM scheme is defined for the momentum configuration where the incoming and outgoing quark momenta are the same p. Since the definition involves the external quark field, which is not gauge invariant, the renormalization condition depends on the gauge. In the RI/MOM scheme, the Landau gauge is chosen.

In the RI/MOM scheme, the wave function renormalization Z_q is fixed by imposing the condition

$$\frac{1}{12i}\,\mathrm{Tr}\left[\frac{\partial\langle S^R(p)\rangle^{-1}}{\partial\not{p}}\right] = Z_q^{-1}\frac{1}{12i}\,\mathrm{Tr}\left[\frac{\partial\langle S(p)\rangle^{-1}}{\partial\not{p}}\right] = 1 \tag{3.3}$$

at $p^2 = \mu^2$ in the chiral limit. Numerically, though, this is not straightforward since it involves a numerical derivative in terms of p_μ. Instead, we obtain Z_q using (3.2) for the axial-vector vertex function $\Lambda_A(p)$ with an input of Z_A obtained through the axial-Ward-Takahashi identity

$$Z_A^{\mathrm{WTI}}\Delta_4\langle A_4(x)\mathcal{O}(0)\rangle = 2m_q\langle P(x)\mathcal{O}(0)\rangle, \tag{3.4}$$

where A_4 and P are the axial-vector current in the time direction and the pseudoscalar density, respectively. Δ_4 denotes the symmetrized difference. This relation must be satisfied as long as the position x of the operator is not too close to the origin, where some interpolating field $\mathcal{O}$ is set. It should be noted that Z_A obtained in this way is taken to be Z_V as well, due to the exact chiral symmetry on the lattice. Once Z_A is fixed from this relation, the wave function renormalization is determined as $Z_q^R(\mu) = Z_A^{\mathrm{WTI}}\Lambda_A(p)$ at $p^2 = \mu^2$.

In practice, we use a pseudoscalar density with a smeared operator for $\mathcal{O}$ and sum over spatial lattice sites. Then, we fit a ratio $2m_q\sum_{\vec{x}}\langle P(\vec{x},t)\mathcal{O}(0)\rangle/\Delta_t\sum_{\vec{x}}\langle A_4(\vec{x},t)\mathcal{O}(0)\rangle$ with time slices $t \geq t_0$, which is large enough to obtain a constant Z_A^{WTI}. For NF2ϵ, setting $m_q = m_{\mathrm{sea}} = 0.002$ and $t_0 = 4$, we obtain

$$Z_A^{\mathrm{WTI}} = 1.3511(12). \tag{3.5}$$

In other ensembles, Z_A^{WTI} is obtained for each sea quark mass with the valence quark mass equal to the sea (up and down) quark mass. Results with $t_0 = 7$ for all ensembles are summarized in Table II, where the second to last row lists the values extrapolated to the chiral limit. In the chiral extrapolation, we assume linear plus quadratic dependence on m_q. Since the local axial-vector current we use on the lattice is not a conserved current at finite lattice spacings, the Ward-Takahashi identity (3.4) may be slightly violated. To be explicit, a discretization effect of the form $a^2 m_q\partial_\mu P$ is possible as an additive correction to A_μ, which leads to the linear dependence on m_q. Including possible quadratic quark mass dependence, we use

$$Z_A^{\mathrm{WTI}}(m_q) = Z_A^{\mathrm{WTI}}(0) + C_1 m_q + C_2 m_q^2 \tag{3.6}$$

by setting the valence quark mass as $m_q = m_{\mathrm{sea}}$ for NF2p and as $m_q = m_{ud}$ for the combined data of NF3p-a and NF3p-b. In Fig. 1, we plot the data and the fit cures for each case. For the case of $N_f = 2 + 1$, we assume independence of Z_A on m_s, which appears only as a sea quark. This assumption is indeed supported by the lattice data at two different m_s.

The vertex function $\Lambda_\Gamma(p)$ is calculated on the lattice at many different momentum values p_{latt}, as listed in Table I. With the overlap fermion, we compute the vertex functions as

$$\Lambda_\Gamma(p_{\mathrm{latt}}) = \frac{1}{12}\,\mathrm{Tr}[\langle\hat{S}_{\mathrm{ov}}(p_{\mathrm{latt}})\rangle^{-1}\langle\hat{S}_{\mathrm{ov}}(p_{\mathrm{latt}})\Gamma\gamma_5\hat{S}_{\mathrm{ov}}^\dagger(p_{\mathrm{latt}})\gamma_5\rangle \times\langle\gamma_5\hat{S}_{\mathrm{ov}}^\dagger(p_{\mathrm{latt}})\gamma_5\rangle^{-1}\Gamma], \tag{3.7}$$

where the quark propagator is effectively given as

$$\hat{S}_{\mathrm{ov}}(p) = \frac{2m_0}{2m_0 - m_q}\left(S_{\mathrm{ov}}(p) - \frac{e^{-ip\cdot x_{\mathrm{src}}}}{2m_0}\right). \tag{3.8}$$

This modification of the quark propagator from $S_{\mathrm{ov}}(p)$, the

TABLE II. Summary of the results of Z_A^{WTI} as a function of m_{sea} or m_{ud} for NF2p, NF3p-a, and NF3p-b. The last two rows show the results of the extrapolation to the chiral limit as described in the text.

NF2p		NF3p-a		NF3p-b	
m_{sea}	Z_A^{WTI}	m_{ud}	Z_A^{WTI}	m_{ud}	Z_A^{WTI}
0.015	1.378 67(61)	0.015	1.389 34(49)	0.015	1.389 68(47)
0.025	1.377 03(45)	0.025	1.387 09(40)	0.025	1.387 00(36)
0.035	1.374 12(40)	0.035	1.384 31(32)	0.035	1.384 08(32)
0.050	1.370 32(33)	0.050	1.380 31(27)	0.050	1.380 19(31)
0.070	1.364 41(31)	0.080	1.371 96(21)	0.100	1.366 58(26)
0.100	1.354 36(29)				
0.00	1.382 22(82)	"Chiral limit": 1.393 60(48)			
(χ^2/dof =	0.43	0.16)			

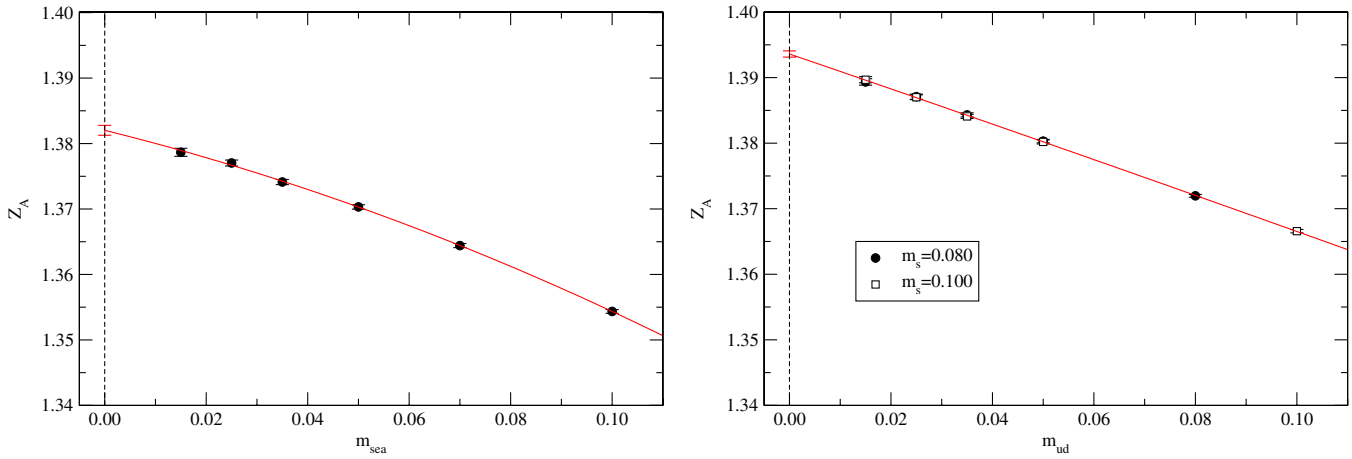

FIG. 1 (color online). Chiral extrapolation of Z_A^{WTI} for NF2p (left panel) and NF3p-a and NF3p-b (right panel).

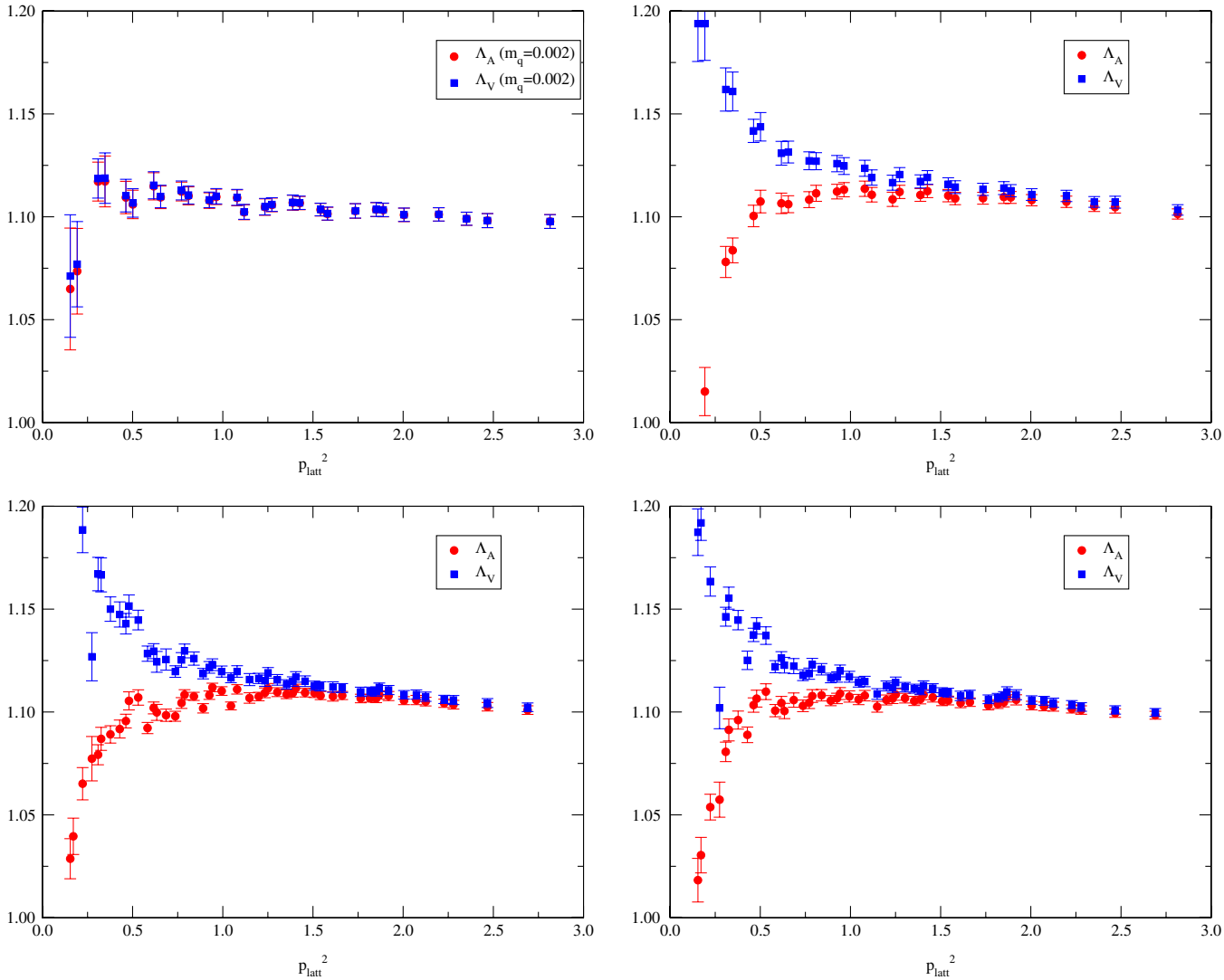

FIG. 2 (color online). Vertex functions $\Lambda_A^{\mathrm{latt}}(p_{\mathrm{latt}})$ (circles) and $\Lambda_V^{\mathrm{latt}}(p_{\mathrm{latt}})$ (squares) at $m_q = 0.002$ for NF2ϵ (upper-left panel), and those in the limit of a massless valence quark ($m_q = 0$) with the sea quark mass fixed at $m_{\mathrm{sea}}(m_{ud}) = 0.015$ for NF2p (upper-right panel), NF3p-a (lower-left panel), and NF3p-b (lower-right panel).

inverse of the overlap operator $D_{\rm ov}(m_q)$, is made in order to incorporate the quark field rotation $q \to (1 - \frac{D_{\rm ov}(0)}{2m_0})q$, $\bar{q} \to \bar{q}$, which is necessary to remove the $\mathcal{O}(a)$ effects from off-shell quantities. In (3.7), we note that $\gamma_5 \hat{S}^\dagger_{\rm ov}(p_{\rm latt})\gamma_5$ cannot be simply replaced by $\hat{S}_{\rm ov}(p_{\rm latt})$ since the left-hand side of (2.4) still depends on the source point $x_{\rm src}$.

B. Vector and axial-vector vertex functions

Results for the vector and axial-vector vertex functions are shown in Fig. 2 as a function of $p^2_{\rm latt} \equiv (\mu a)^2$. In the figure, panels from NF2p, NF3p-a, and NF3p-b show the data from the lightest $m_{\rm sea}$ or m_{ud}. The chiral symmetry implies that these two functions become identical in the massless limit unless the symmetry is spontaneously broken. With exact chiral symmetry of the overlap fermion, this should be the case even at finite lattice spacings. The result in the ϵ regime (NF2ϵ, upper-left panel) clearly shows this behavior, which is consistent with the absence of spontaneous symmetry breaking on a finite volume lattice.

The other three panels, that are obtained in the p regime, show the splitting between the vector and the axial-vector channels. The numerical data in these plots are naively extrapolated to the chiral limit of the valence quarks by assuming a linear dependence on m_q, but the qualitative picture remains unchanged for each valence quark mass.

This inconsistency among the vector and axial-vector currents may be explained as an effect of spontaneously broken chiral symmetry. Even on a finite volume lattice,

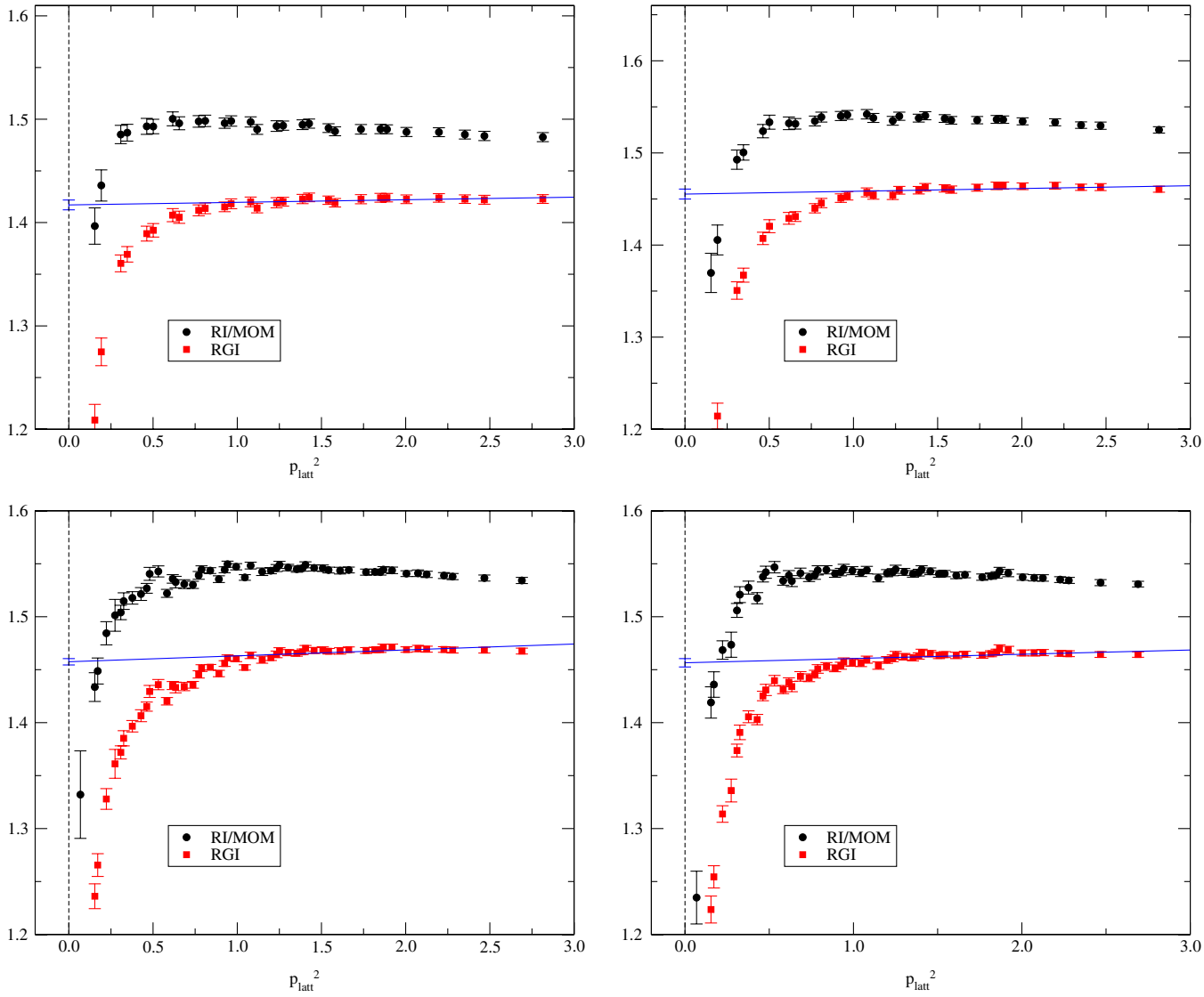

FIG. 3 (color online). Quark field renormalization factor Z_q as a function of $p^2_{\rm latt}$. For NF2p, NF3p-a, and NF3p-b, data at $m_{\rm sea}(m_{ud}) = 0.015$ are plotted as an example. Results in the RI/MOM scheme are shown by circles, while those in RGI are plotted by squares.

TABLE III. Numerical results for the quark wave function renormalization factor Z_q. The values in the RGI definition Z_q^{RGI} and those defined in the $\overline{\mathrm{MS}}$ scheme at $\mu = 2$ GeV, $Z_q^{\overline{\mathrm{MS}}}(2\ \mathrm{GeV})$ are listed for each sea quark mass.

$m_{\mathrm{sea}}(m_{ud})$		Z_q^{RGI}	$Z_q^{\overline{\mathrm{MS}}}(2\ \mathrm{GeV})$
NF2ϵ,	0.002	1.4170(47)	1.4799(50)
NF2p	0.015	1.4540(54)	1.5186(56)
	0.025	1.4503(51)	1.5147(53)
	0.035	1.4479(53)	1.5122(56)
	0.050	1.4486(49)	1.5129(51)
	0.070	1.4442(51)	1.5083(54)
	0.100	1.4500(59)	1.5143(62)
	0.000	1.4526(30)	1.5170(31)
	(χ^2/dof	0.33	0.33)
NF3p-a	0.015	1.4575(30)	1.5279(31)
	0.025	1.4641(38)	1.5348(40)
	0.035	1.4660(51)	1.5368(54)
	0.050	1.4528(27)	1.5230(29)
	0.080	1.4590(37)	1.5294(39)
NF3p-b	0.015	1.4565(40)	1.5269(42)
	0.025	1.4585(32)	1.5290(34)
	0.035	1.4555(28)	1.5258(29)
	0.050	1.4467(30)	1.5166(31)
	0.100	1.4578(55)	1.5283(57)
"Chiral limit":		1.4592(29)	1.5296(31)
	(χ^2/dof	2.20	2.20)

spontaneous symmetry breaking induces a nonzero value of the chiral condensate $-\langle\bar{q}q\rangle \equiv \Sigma$ as long as the quark mass is much larger than a typical scale $1/\Sigma V$. An operator product expansion (OPE) analysis [3] suggests that there are contributions of the form $\Lambda_{\mathrm{QCD}}^2/p^2$ and $m\Lambda_{\mathrm{QCD}}/p^2$ to the difference $\Lambda_A(p) - \Lambda_V(p)$. These contributions are induced when the momentum assignment for the three-point function gives vanishing momentum transfer at the vertex. Namely, when the incoming and outgoing momenta are identical as in the RI/MOM-scheme momentum setup, which is called the "exceptional momenta," the higher dimensional terms in OPE like $(\bar{q}q)^2/p^6$ (with some gamma matrices inserted in the numerator) may lead to a much larger contribution of the form $\langle(\bar{q}q)^2\rangle/(\Lambda_{\mathrm{QCD}}^4 p^2)$, which remains in the chiral limit in contrast to the lower order contributions m^2/p^2 or $m\langle\bar{q}q\rangle/p^4$ [3]. This problem can be avoided by choosing other momentum configurations, such as the RI/sMOM scheme considered in [24].

We do not go into the details of this problem. But, since the effect becomes statistically significant only below $p_{\mathrm{latt}}^2 \sim 1.0$–$1.5$ for the vector and axial-vector channels, we simply use the region that is not largely affected by this effect in the following analysis.

The quark field renormalization factor $Z_q(\mu)$ can be obtained from $\Lambda_A(p)$ by multiplying the axial-current renormalization constant Z_A^{WTI} as determined from the Ward-Takahashi identity. The results are shown in Fig. 3 by filled circles as a function of p_{latt}^2. The different panels represent the data from the ensembles NF2ϵ, NF2p, NF3p-a, and NF3p-b, respectively. By multiplying the matching factor $1/w_q^{\mathrm{RI/MOM}}(q)$ at the four-loop level as defined in the Appendix, we may define the renormalization group invariant (RGI) quantity, which is also scheme independent. Our numerical results, plotted by squares in Fig. 3, clearly show the expected scale independence. Since we expect discretization effects proportional to $a^2 p_{\mathrm{latt}}^2$, we fit the lattice data above $(p_{\mathrm{latt}})^2 = 1.0$ by a linear function and obtain the result for Z_q^{RGI} from an intercept at $p_{\mathrm{latt}}^2 = 0$. The lattice data below $a^2 p_{\mathrm{latt}}^2 \simeq 1.0$ are largely affected by the effect of spontaneously broken chiral symmetry and deviate from the linear behavior as expected.

The results for Z_q^{RGI} are listed in Table III. Also listed are the results converted to the $\overline{\mathrm{MS}}$ scheme at $\mu = 2$ GeV using the four-loop level matching constant $w_q^{\overline{\mathrm{MS}}}(\mu)$ defined in the Appendix.

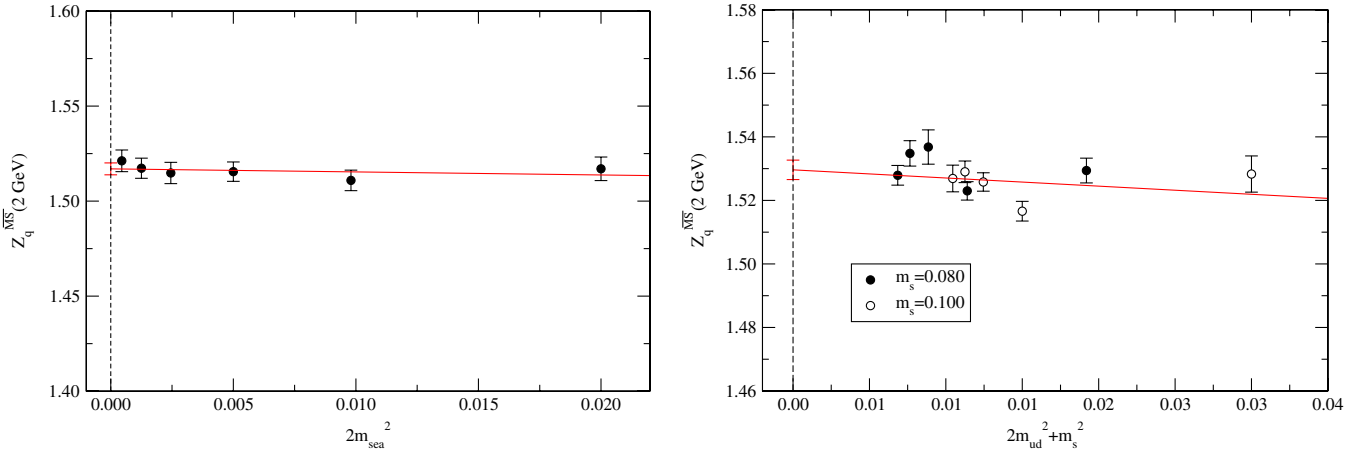

FIG. 4 (color online). Chiral extrapolation of $Z_q^{\overline{\mathrm{MS}}}(2\ \mathrm{GeV})$ on the NF2p (left panel), NF3p-a (right panel, filled symbols), and NF3p-b (right panel, open symbols) lattices.

So far, the results are given at each sea quark mass after taking the chiral limit of valence quarks. The chiral limit of sea quarks can be taken by assuming that the sea quark mass dependence has the form $Z(1 + 2c^{(2)}m_{\rm sea}^2)$ (for NF2p) or $Z(1 + c^{(3)}(2m_{ud}^2 + m_s^2))$ (for NF3p-a and NF3p-b). The coefficients $c^{(2)}$ and $c^{(3)}$ are numerical constants depending on the number of flavors. The linear term in $m_{\rm sea}$ (or in m_{ud}) should not remain for the quantities irrelevant to chiral symmetry breaking. Figure 4 shows the chiral extrapolation of $Z_q^{\overline{\rm MS}}(2\ {\rm GeV})$ for both NF2p and NF3p-a/NF3p-b. We do not observe any significant sea quark mass dependence. The chiral extrapolation should therefore be very stable. The results are listed in Table III.

C. Scalar and pseudoscalar vertex functions

In Fig. 5, the momentum dependence of the scalar vertex function $\Lambda_S^{\rm latt}(p_{\rm latt})$ (filled symbols) and the pseudoscalar vertex function $\Lambda_P^{\rm latt}(p_{\rm latt})$ (open symbols) is shown for each ensemble. For the data in the ϵ regime (circles in the upper-left panel), we observe an excellent agreement between $\Lambda_S(p)$ (filled symbols) and $\Lambda_P(p)$ (open symbols), which is expected from the exact chiral symmetry of the overlap fermion. On the other hand, once the valence quark mass m_q is out of the ϵ regime (the data at $m_q = 0.015$, 0.025, and 0.035 are plotted by squares, diamonds, and triangles, respectively), we find large disagreement between $\Lambda_S(p)$ and $\Lambda_P(p)$.

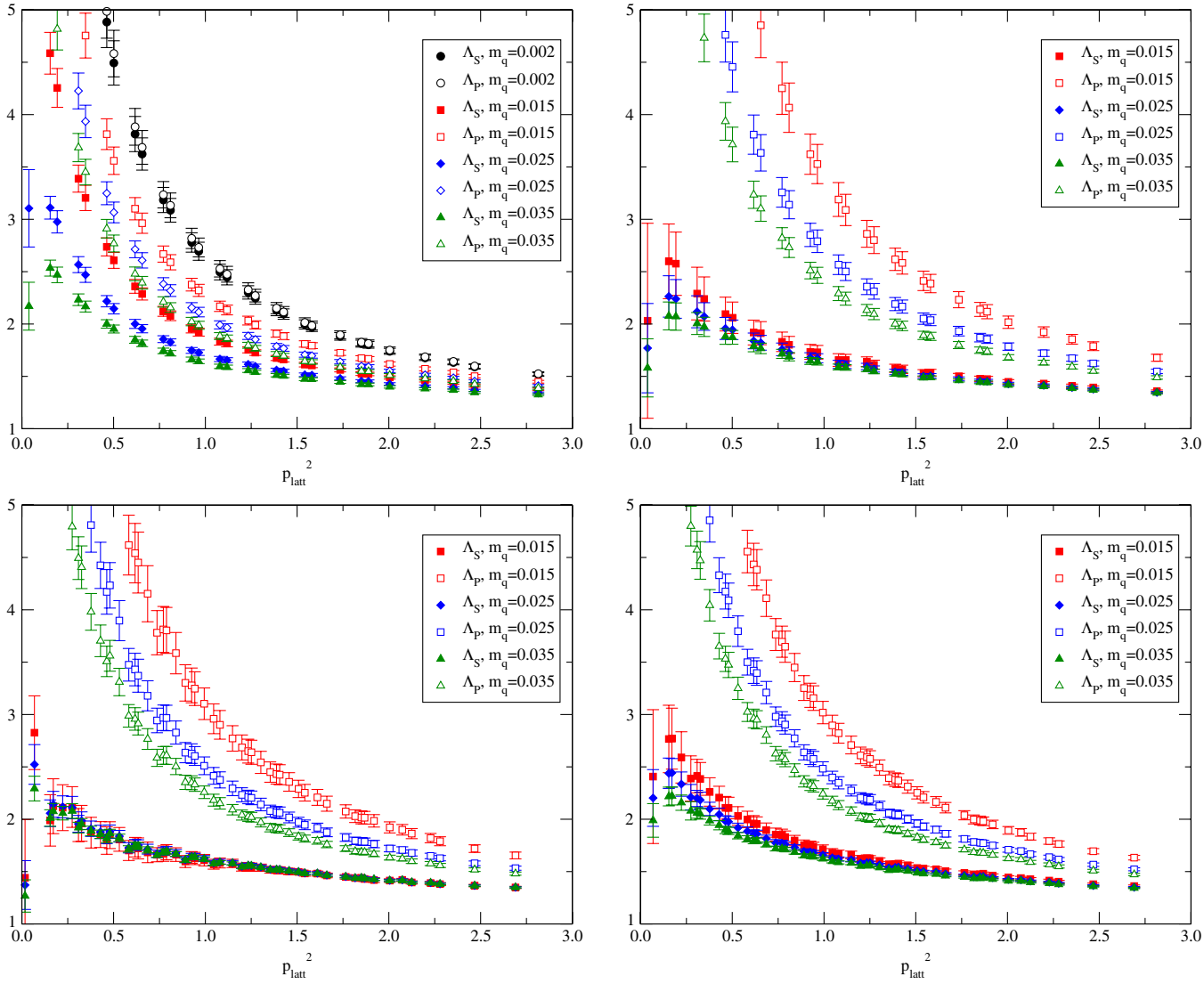

FIG. 5 (color online). Vertex functions $\Lambda_S^{\rm latt}(p_{\rm latt})$ (filled symbols) and $\Lambda_P^{\rm latt}(p_{\rm latt})$ (open symbols). The data are shown for NF2ϵ (upper-left panel), NF2p (upper-right panel), NF3p-a (lower-left panel), and NF3p-b (lower-right panel) as functions of $p_{\rm latt}^2$. In each panel, data at $m_q = 0.015$, 0.025, and 0.035 are shown by squares, diamonds, and triangles, respectively. For NF2ϵ, data at $m_q = 0.002$ are shown as well by circles. For NF2p, NF3p-a, and NF3p-b, data at the lightest sea quark $m_{\rm sea}(m_{ud}) = 0.015$ are plotted as an example.

This observation again indicates the effect of spontaneous chiral symmetry breaking. From the OPE analysis one expects that this effect is more significant than in $\Lambda_V(p)$ and $\Lambda_A(p)$, because the violation is enhanced by an inverse quark mass as discussed below. One has to subtract this effect in order to extract the renormalization constants because its matching is based on the continuum perturbation theory that does not contain nonperturbative effects.

We consider the quark mass dependence of $\Lambda_S(p)$ and $\Lambda_P(p)$ using OPE along the lines of the analysis in [2]. Using the vector and axial-vector Ward-Takahashi identities, one may obtain relations between the vertex functions and the inverse quark propagators as [25]

$$\Lambda_S(p) = \frac{1}{12}\frac{\partial\,\mathrm{Tr}\langle S(p)\rangle^{-1}}{\partial m_q}, \tag{3.9}$$

$$\Lambda_P(p) = \frac{1}{12}\frac{\mathrm{Tr}\langle S(p)\rangle^{-1}}{m_q}. \tag{3.10}$$

On the lattice we use the improved overlap quark propagator $\hat{S}_{\mathrm{ov}}(p)$ in place of $S(p)$. From OPE the inverse quark propagator $\mathrm{Tr}\langle S(p)\rangle^{-1}$ may be written as [26]

$$\frac{1}{12}\mathrm{Tr}\langle S(p)\rangle^{-1} = C\cdot\frac{\langle\bar{q}q\rangle}{p^2} + Z_q Z_m m_q + \cdots \tag{3.11}$$

in the large p^2 regime. The effect of chiral symmetry breaking is picked up through the chiral condensate $\langle\bar{q}q\rangle$, and C is a perturbatively calculable constant. At the one-loop level, $C = 4\pi\alpha_s/3$. As in the case of the vector and axial-vector vertex functions, the effects from higher dimensional operators, such as $\langle(\bar{q}q)^2\rangle$, may also exist. They are usually suppressed by additional powers of $1/p^2$, but due to the lack of momentum injection, the suppression may not work in the case of the inverse quark propagator or in the case of the vertex functions at zero momentum transfer. We therefore leave C as an unknown constant instead of using the perturbatively known value.

Then, using the relations (3.9) and (3.10), we may evaluate the effect of the chiral condensate on the vertex functions as

$$\Lambda_S(p) = \frac{C}{p^2}\frac{\partial\langle\bar{q}q\rangle}{\partial m_q} + Z_q Z_m + \cdots, \tag{3.12}$$

$$\Lambda_P(p) = \frac{C}{p^2}\frac{\langle\bar{q}q\rangle}{m_q} + Z_q Z_m + \cdots. \tag{3.13}$$

From these expressions, one sees an enhancement in the low p^2 region due to the chiral condensate only for the pseudoscalar channel, while the scalar channel should not be affected too much because of a derivative with respect to m_q rather than a factor $1/m_q$.

The quark mass dependence of the condensate $\langle\bar{q}q\rangle$ is not a trivial issue, since it has effects from both ultraviolet and infrared origins. Since the operator $\bar{q}q$ contains quadratic divergence of the form m_q/a^2 apart from the chiral limit, the chiral condensate $\langle\bar{q}q\rangle$ directly calculated on the lattice contains unphysical, large m_q dependence. It has to be subtracted before the analysis using (3.12) and (3.13), because the formulas are obtained as an expansion around the chiral limit.

In the infrared regime, the chiral condensate has a nontrivial quark mass dependence, especially in a finite volume. First, because of the pion-loop effects, the chiral condensate develops the chiral logarithm of the form $m_q \ln m_q$ with known coefficients [27]. On a finite volume lattice, the quark mass dependence becomes more complicated. Namely, once the quark mass enters the ϵ regime, the mass dependence is no longer governed by the simple chiral logarithm, but given by the formula recently developed in [28].

In our analysis, instead of using the formula in [28] we calculate the condensate using its eigenvalue decomposition by making use of the low eigenmodes obtained on the same ensembles. For each lattice configuration, we define

$$(\bar{q}q)^{(N)} = \frac{1}{L_s^3 L_t}\sum_{i=1}^{N}\frac{2m_q}{m_q^2 + \hat{\lambda}_i^*\hat{\lambda}_i}, \tag{3.14}$$

where $\hat{\lambda}_i$ is an eigenvalue of the massless overlap-Dirac operator, which satisfies the eigenequation

$$D_{\mathrm{ov}}(0)\left(1 - \frac{D_{\mathrm{ov}}(0)}{2m_0}\right)^{-1} u_i(x) = \hat{\lambda}_i u_i(x) \tag{3.15}$$

with $u_i(x)$ an eigenvector. In (3.14) we use the fact that the eigenvalues appear as complex conjugate pairs. The normalization in (3.14) contains the lattice volume $L_s^3 L_t$.

We truncate the sum in (3.14) at the Nth eigenvalue, which may be considered as a "renormalization scheme" to define the divergent operator $\bar{q}q$. Here, N plays the role of the ultraviolet cutoff. After taking an ensemble average, we denote the chiral condensate thus defined as $\langle\bar{q}q\rangle^{(N)}$. In the course of our project, we calculate and store the low-lying eigenvalues and eigenvectors of the overlap-Dirac operator. In addition to the calculation of the truncated chiral condensate (3.14), these eigenmodes can be used to precondition the solvers, to average over source points, or to construct disconnected diagrams in the calculations of physical observables [13,15,29]. The numbers of the stored low modes for each configuration are listed in Table I.

From a dimensional analysis, the quark mass dependence of $\langle\bar{q}q\rangle^{(N)}$ may be parametrized as

$$\langle\bar{q}q\rangle^{(N)} = \langle\bar{q}q\rangle^{(\mathrm{subt})} + c_1^{(N)}\frac{m_q}{a^2} + c_2^{(N)} m_q^3. \tag{3.16}$$

Because of the exact chiral symmetry of the overlap fermion, there is no leading power divergence of the order $1/a^3$, and the term behaves as m_q^2/a is also absent. Although the cubic term $c_2^{(N)} m_q^3$ in (3.16) may accompany a logarithm $\ln m_q$, we omit it for simplicity as the m_q^3 term

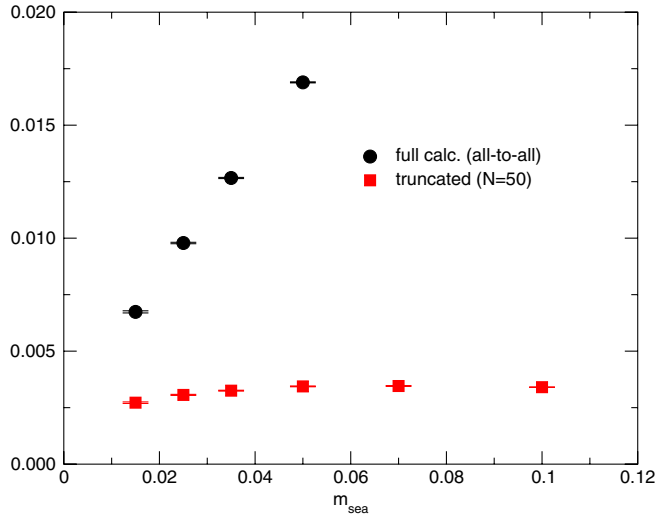

FIG. 6 (color online). Comparison between $\langle\bar{q}q\rangle$ obtained from all-to-all propagators (circles) and $\langle\bar{q}q\rangle^{(N=50)}$ (squares) as a function of $m_{\rm sea} = m_q$. The data obtained on NF2p are shown.

itself is a minor correction. The subtracted condensate $\langle\bar{q}q\rangle^{(\rm subt)}$ is then free from power divergences, but could still contain nondivergent m_q dependence, such as the chiral logarithm.

In Fig. 6, we compare a "full" calculation of $\langle\bar{q}q\rangle$ (circles) corresponding to $N = 12L_s^3L_t$ and $\langle\bar{q}q\rangle^{(N=50)}$. The full calculation contains the contributions of all eigenmodes which are evaluated by a stochastic method. (Our setup is explained in [29].) The data on the NF2p lattice with sea and valence quark masses set equal are shown as an example. The results clearly show that the divergent term m_q/a^2 in (3.16) dominates the full condensate, and it seems difficult to extract $\langle\bar{q}q\rangle^{(\rm subt)}$ from these data alone. The truncated condensate, on the other hand, does not have that strong m_q dependence, but both the m_q/a^2 and m_q^3 terms are still visible.

We now try to extract the nondivergent term $\langle\bar{q}q\rangle^{(\rm subt)}$ using (3.16). In Figs. 7–9 (left panels) we plot the truncated condensate $\langle\bar{q}q\rangle^{(N)}$ as a function of the valence quark mass with three or four different values of N. The data are shown for individual lattice ensembles (NF2ϵ, NF2p, NF3p-a, and NF3p-b); except for NF2ϵ, the results at the lightest sea quark are shown as an example. The truncated condensate can be constructed at arbitrary values of the valence quark mass m_q without extra computational costs. In order to see the ultraviolet behavior, we plot in the mass region up to $m_q = 0.20$, which is twice as big as the largest simulated sea quark mass.

When we fit the lattice data to (3.16), we take five or six representative points of m_q in the range $0.10 \le m_q \le 0.18$ for NF2ϵ and NF2p or $0.10 \le m_q \le 0.20$ for NF3p-a and NF3p-b. The upper limit is chosen such that $|\hat{\lambda}_N| > m_q$ for the given N. Otherwise, we do not expect the ultraviolet behavior (3.16). In this rather heavy mass region, we do not expect additional mass dependence from the infrared origin, and we simply set $-\langle\bar{q}q\rangle^{(\rm subt)} = \Sigma$ with Σ a constant.

The fit results are shown in Figs. 7–9 (left panels) by dashed curves. In the right panels of these figures, the subtracted condensates $\langle\bar{q}q\rangle^{(\rm subt)} = \langle\bar{q}q\rangle^{(N)} - c_1^{(N)}/a^2 m_q - c_2^{(N)} m_q^3$ for the same choices of N as the left panels are

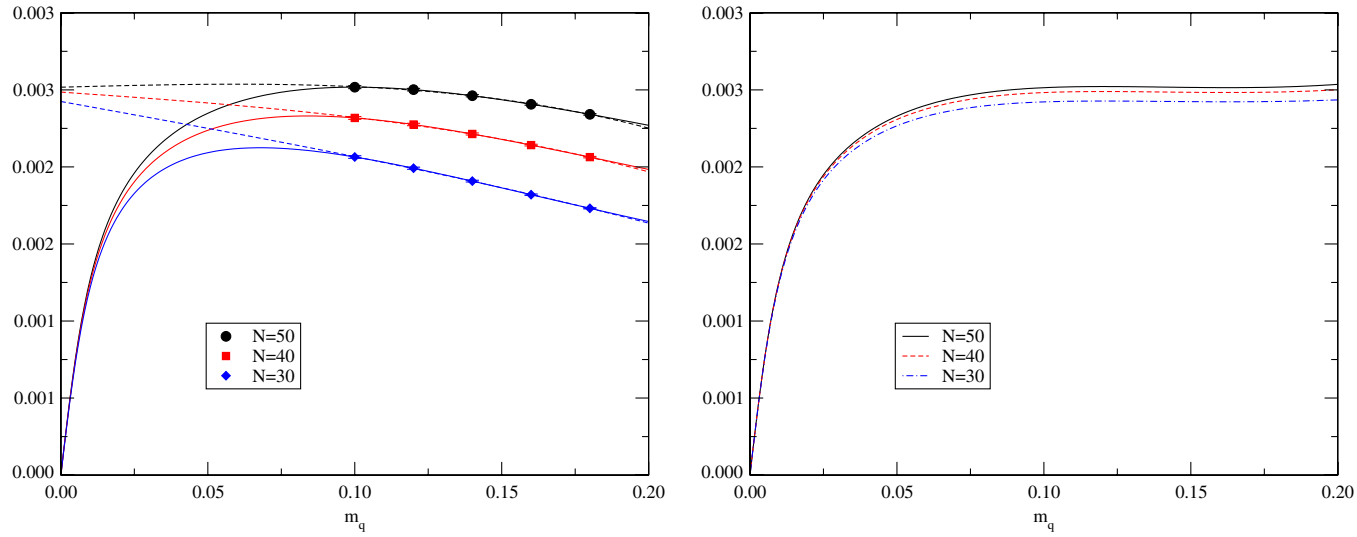

FIG. 7 (color online). Subtraction of the power divergence in the chiral condensate. The left panel shows $\langle\bar{q}q\rangle^{(N)}$ calculated on the NF2ϵ lattice as a function of the valence quark mass m_q (solid curves). The number of low modes included are $N = 50$, 40, and 30 from top to bottom. The solid curves are data constructed from calculated eigenvalues, and the points with error bars are representative points used in our fit. The fit curves according to (3.16) are shown by dashed curves. The right panel represents the subtracted condensate $\langle\bar{q}q\rangle^{(\rm subt)}$.

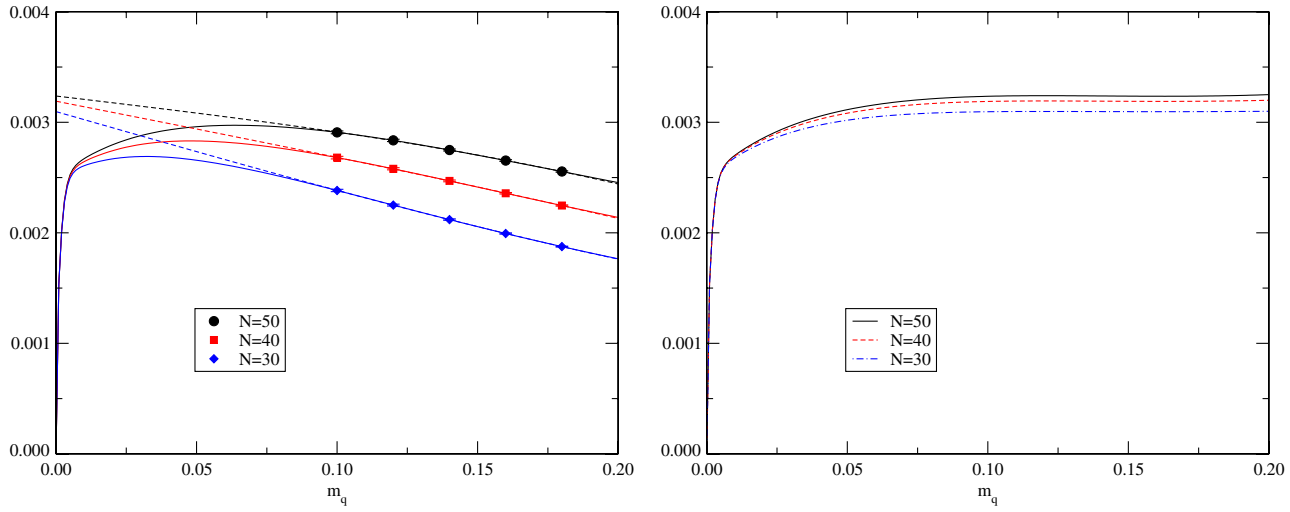

FIG. 8 (color online). Same as Fig. 7 but for NF2p at $m_{\text{sea}} = 0.015$.

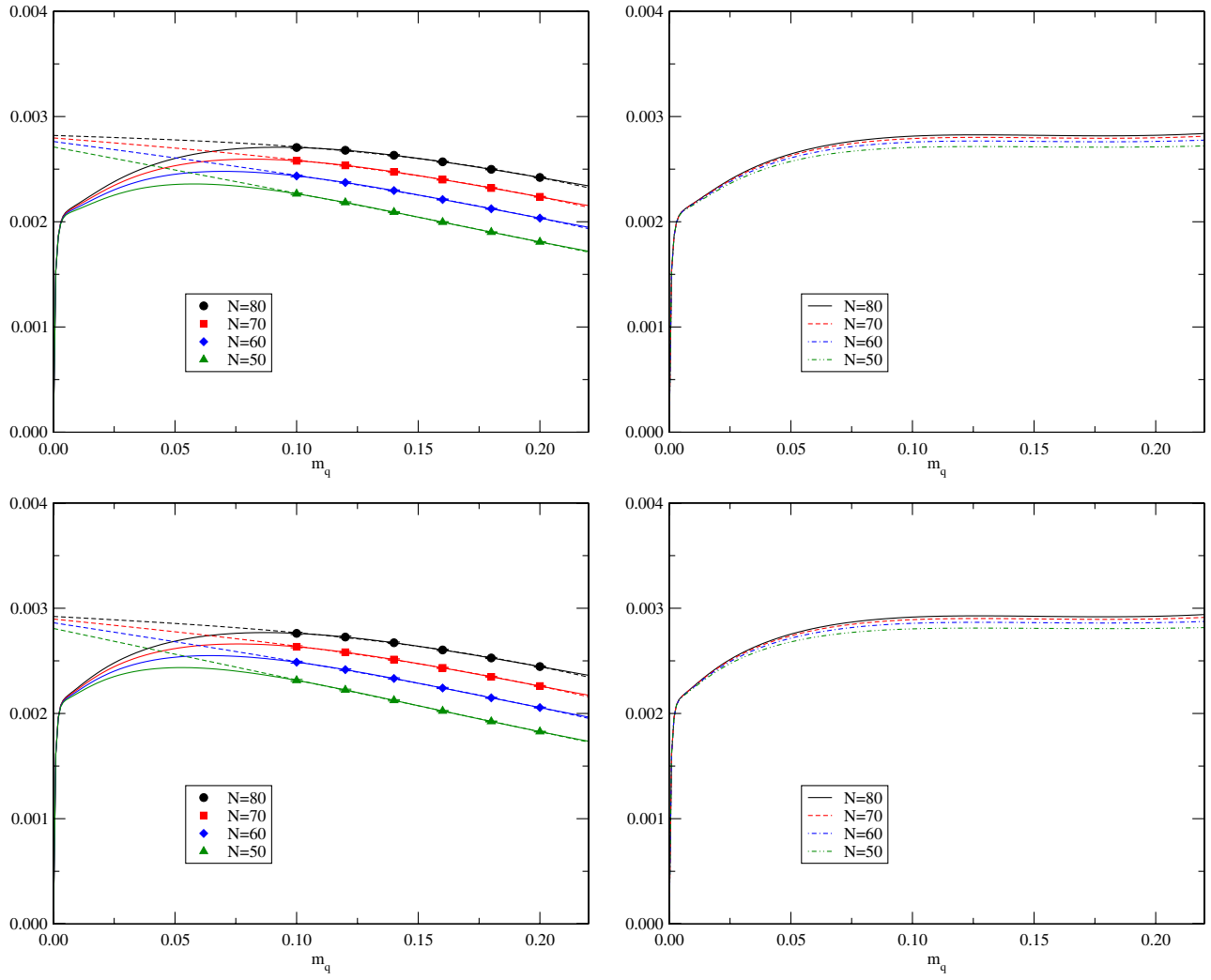

FIG. 9 (color online). Same as Fig. 7 but for NF3p-a (top panels) and NF3p-b (bottom panels) at $m_{ud} = 0.015$. The number of low modes included are $N = 80$, 70, 60, and 50 from top to bottom.

shown. We observe that the subtracted condensate depends on N very mildly to a few percent order. It implies that our subsequent analysis using $\langle\bar{q}q\rangle^{(N)}$ with the maximal N may contain a small systematic error due to the truncation of N. We discuss this point and estimate the error in Sec. III D.

We use $\langle\bar{q}q\rangle^{(\mathrm{subt})}$ thus obtained at each sea quark mass as a function of the valence quark mass in the analysis of the scalar and pseudoscalar vertex functions, (3.12) and (3.13), respectively. The valence quark mass dependence of $\Lambda_S^{\mathrm{latt}}(p_{\mathrm{latt}})$ and $\Lambda_P^{\mathrm{latt}}(p_{\mathrm{latt}})$ at four representative values of p_{latt}^2 is plotted in Fig. 10. We find that both the scalar (filled symbols) and pseudoscalar (open symbols) vertices are nicely described by the fit curves according to (3.12) and (3.13) supplemented by the measured $\langle\bar{q}q\rangle^{(\mathrm{subt})}$. In particular, as seen near the chiral limit of the NF2ϵ data, the fit curves precisely reproduce the agreement of $\Lambda_S^{\mathrm{latt}}(p_{\mathrm{latt}})$ and $\Lambda_P^{\mathrm{latt}}(p_{\mathrm{latt}})$ in the ϵ regime, which is not expected when $\langle\bar{q}q\rangle$ is treated as a mass-independent constant.

In addition to (3.12) and (3.13), quadratic mass dependence is possible for the vertex functions $\Lambda_S^{\mathrm{latt}}(p_{\mathrm{latt}})$ and $\Lambda_P^{\mathrm{latt}}(p_{\mathrm{latt}})$:

$$\Lambda_S(p_{\mathrm{latt}}) = \frac{C}{p^2}\frac{\partial\langle\bar{q}q\rangle}{\partial m_q} + Z_q Z_m + B_S m_q^2, \tag{3.17}$$

$$\Lambda_P(p_{\mathrm{latt}}) = \frac{C}{p^2}\frac{\langle\bar{q}q\rangle}{m_q} + Z_q Z_m + B_P m_q^2. \tag{3.18}$$

From a combined fit of the valence quark mass dependence, we obtain the parameters C, $Z_q Z_m$, B_P, and B_S at

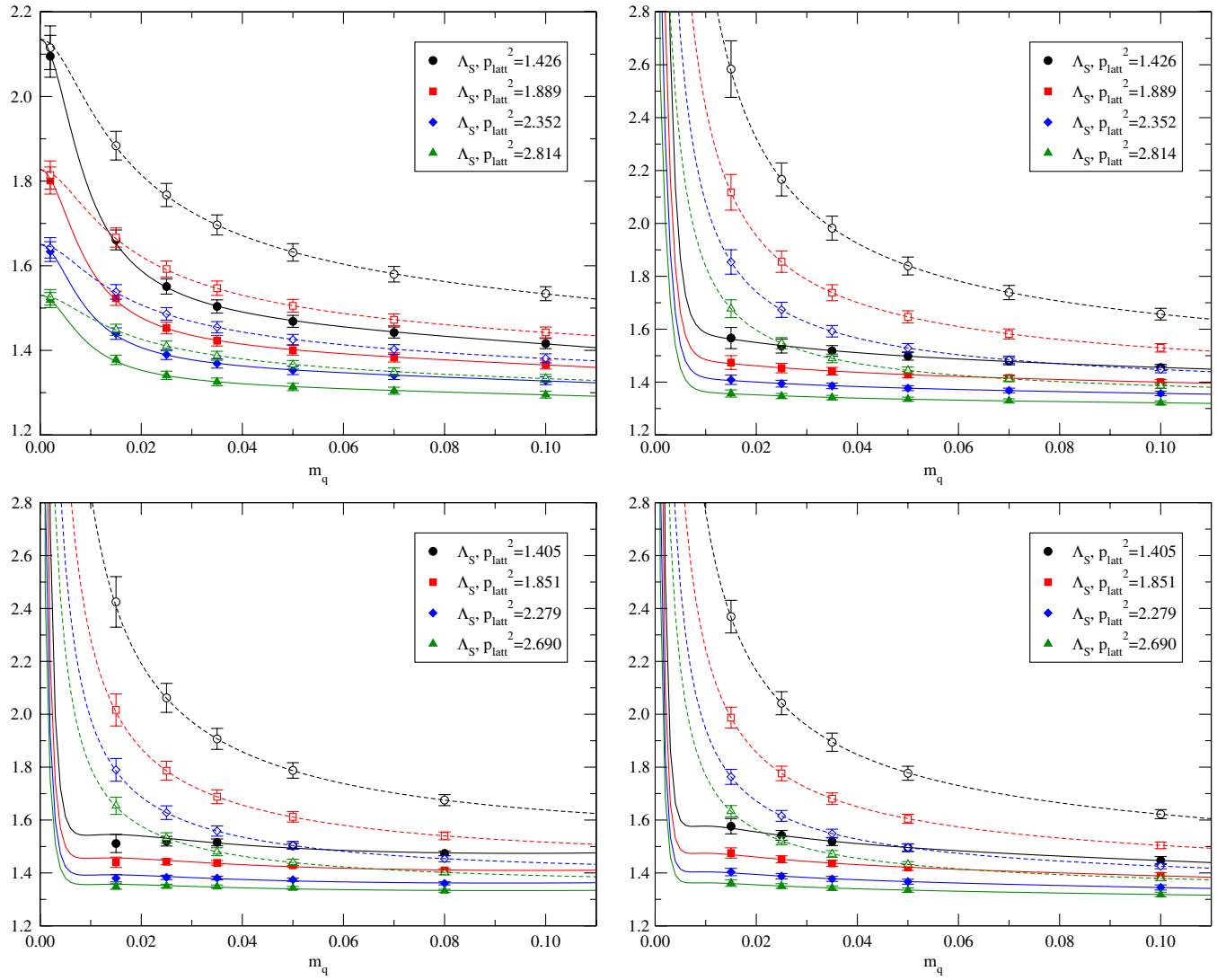

FIG. 10 (color online). Vertex functions $\Lambda_S^{\mathrm{latt}}(p_{\mathrm{latt}})$ (filled symbols) and $\Lambda_P^{\mathrm{latt}}(p_{\mathrm{latt}})$ (open symbols). The data are shown for the NF2ϵ (upper-left panel), NF2p (upper-right panel), NF3p-a (lower-left panel), and NF3p-b (lower-right panel) lattices as functions of m_q. In each panel, data at selected values of p_{latt}^2 and their fit curves are presented. For NF2p, NF3p-a, and NF3p-b, data with a fixed sea quark mass $m_{\mathrm{sea}}(m_{ud}) = 0.015$ are plotted as an example.

TABLE IV. Parameters in the simultaneous fit of $\Lambda_S^{\rm latt}$ and $\Lambda_P^{\rm latt}$ for NF2ϵ. Results at representative values of lattice momenta are listed.

$p^2_{\rm latt}$	C	Z_qZ_m	B_S	B_P	χ^2/dof
1.426	5.92(40)	1.443(16)	−3.10(90)	−1.35(34)	0.025
1.889	5.01(32)	1.384(13)	−2.08(62)	−0.85(25)	0.017
2.352	4.32(28)	1.342(11)	−1.60(48)	−0.76(22)	0.016
2.814	3.78(26)	1.3060(92)	−1.23(36)	−0.65(15)	0.017

each value of $p^2_{\rm latt}$. Numerical results are listed in Tables IV, V, VI, and VII for each sea quark mass of the NF2ϵ, NF2p, NF3p-a, and NF3p-b lattices. We find that the values of C depend on p^2 only mildly, which is consistent with the logarithmic dependence through α_s.

D. Renormalization constants

From the fits described in the previous subsections, we obtain the numerical results for Z_q and $Z_qZ_m = Z_q/Z_S$ for each available value of $p_{\rm latt}$. From a similar analysis, we also obtain $\Lambda_T = Z_qZ_T^{-1}$, which does not depend on the quark mass significantly. We combine these results with $Z_q(\mu)$ to obtain $Z_m^{\rm RI/MOM}(\mu) = 1/Z_S^{\rm RI/MOM}(\mu)$ and $Z_T^{\rm RI/MOM}(\mu)$ as functions of the renormalization scale μ.

The results are plotted in Figs. 11 and 12 for Z_m and Z_T, respectively. Filled black symbols representing the numerical data for the RI/MOM scheme clearly show a scale (or $p^2_{\rm latt}$) dependence. This dependence can partly be absorbed by the perturbatively calculated matching factor $w_{\mathcal{O}}^{\rm RI/MOM}(\mu)$ ($\mathcal{O} = m$ or T) to the RGI values as in the case of Z_q. The perturbative results for $w_{\mathcal{O}}^{\rm RI/MOM}(\mu)$ and $w_{\mathcal{O}}^{\overline{\rm MS}}(\mu)$ are summarized in the Appendix.

The numerical data for $Z_{\mathcal{O}}^{\rm RGI} = Z_{\mathcal{O}}^{\rm RI/MOM}(p_{\rm latt})/w_{\mathcal{O}}^{\rm RI/MOM}(p_{\rm latt})$ are also shown in Figs. 11 and 12. We find that the scale dependence is largely absorbed at least above $(p_{\rm latt})^2 \simeq 1$, as expected. Below $(p_{\rm latt})^2 \simeq 1$ the perturbative estimate of $w_{\mathcal{O}}^{\rm RI/MOM}(p)$ becomes less precise even though three- or four-loop calculations are used. The remaining

TABLE V. Same as Table IV but for NF2p.

$m_{\rm sea}$	$p^2_{\rm latt}$	C	Z_qZ_m	B_S	B_P	χ^2/dof
0.015	1.426	8.48(83)	1.472(22)	−2.0(1.9)	−0.80(91)	0.004
	1.889	7.16(68)	1.412(16)	−1.5(1.3)	−0.57(66)	0.005
	2.352	6.19(59)	1.366(11)	−1.01(95)	−0.35(46)	0.005
	2.814	5.31(51)	1.3271(89)	−0.65(75)	−0.18(38)	0.004
0.025	1.426	7.43(39)	1.497(20)	−5.3(1.1)	−2.21(49)	0.139
	1.889	6.29(32)	1.429(15)	−3.53(76)	−1.33(35)	0.084
	2.352	5.43(26)	1.380(13)	−2.66(56)	−1.07(25)	0.071
	2.814	4.61(23)	1.341(10)	−2.18(43)	−0.96(23)	0.094
0.035	1.426	8.57(91)	1.446(24)	−0.2(2.0)	−0.1(1.1)	0.190
	1.889	7.37(77)	1.392(17)	0.1(1.4)	0.11(71)	0.179
	2.352	6.23(61)	1.353(13)	−0.13(92)	−0.02(48)	0.133
	2.814	5.40(56)	1.317(11)	0.00(76)	0.09(43)	0.129
0.050	1.426	9.00(58)	1.469(21)	−1.3(1.5)	−0.86(63)	0.021
	1.889	7.61(49)	1.419(15)	−1.1(1.1)	−0.54(48)	0.014
	2.352	6.54(42)	1.377(12)	−0.95(81)	−0.59(36)	0.019
	2.814	5.60(37)	1.340(10)	−0.89(63)	−0.61(31)	0.047
0.070	1.426	7.33(54)	1.476(19)	−5.1(1.4)	−2.19(63)	0.303
	1.889	6.23(45)	1.412(14)	−3.56(99)	−1.50(45)	0.267
	2.352	5.36(40)	1.363(11)	−2.61(78)	−1.03(38)	0.228
	2.814	4.56(34)	1.3262(93)	−2.23(58)	−0.94(30)	0.249
0.100	1.426	8.24(61)	1.444(19)	−1.9(1.5)	−1.09(62)	0.008
	1.889	6.99(53)	1.394(14)	−1.4(1.1)	−0.81(46)	0.014
	2.352	6.04(47)	1.351(12)	−0.92(88)	−0.51(42)	0.003
	2.814	5.18(42)	1.316(10)	−0.72(74)	−0.32(39)	0.004

TABLE VI. Same as Table IV but for NF3p-a.

m_{ud}	$p^2_{\rm latt}$	C	$Z_q Z_m$	B_S	B_P	χ^2/dof
0.015	1.405	9.00(98)	1.445(21)	2.3(2.8)	1.3(1.5)	0.345
	1.851	7.58(82)	1.393(14)	1.3(1.9)	0.9(1.1)	0.248
	2.279	6.65(72)	1.347(10)	1.2(1.5)	0.87(86)	0.276
	2.690	5.86(62)	1.3228(83)	0.8(1.1)	0.55(58)	0.194
0.025	1.405	7.18(52)	1.477(14)	−3.5(1.4)	−1.59(60)	0.046
	1.851	6.14(44)	1.418(11)	−2.77(94)	−1.41(42)	0.056
	2.279	5.25(37)	1.3661(93)	−2.07(72)	−1.03(35)	0.046
	2.690	4.64(32)	1.3379(78)	−1.86(53)	−0.92(26)	0.065
0.035	1.405	7.21(54)	1.495(19)	−3.3(2.0)	−1.90(81)	0.018
	1.851	6.19(46)	1.427(15)	−2.1(1.5)	−1.17(58)	0.018
	2.279	5.36(40)	1.376(12)	−1.6(1.1)	−0.91(48)	0.015
	2.690	4.75(36)	1.3448(97)	−1.20(88)	−0.58(38)	0.010
0.050	1.405	7.88(56)	1.444(16)	−0.2(1.9)	−0.34(82)	0.098
	1.851	6.80(52)	1.391(12)	0.0(1.5)	−0.03(72)	0.099
	2.279	5.82(44)	1.3464(92)	0.0(1.1)	0.14(52)	0.086
	2.690	5.27(43)	1.3216(80)	0.08(98)	0.10(48)	0.075
0.080	1.405	9.24(67)	1.449(19)	−0.7(2.6)	−9.35(78)	0.211
	1.851	8.00(59)	1.395(13)	−0.2(1.9)	−5.81(59)	0.226
	2.279	6.81(50)	1.352(10)	−0.1(1.4)	−3.93(47)	0.189
	2.690	6.06(44)	1.3296(86)	−0.2(1.1)	−3.01(38)	0.138

scale dependence above $(p_{\rm latt})^2 \simeq 1$ is ascribed to the discretization effect of $O(a^2)$. We therefore extrapolate the data for $Z_{\mathcal{O}}^{\rm RGI}$ above $(p_{\rm latt})^2 = 1$ to the vanishing $(p_{\rm latt})^2$ limit, assuming a linear dependence on $(p_{\rm latt})^2$, which is shown by solid lines in Figs. 11 and 12.

The renormalization constants in the $\overline{\rm MS}$ scheme are obtained as $Z_{\mathcal{O}}^{\overline{\rm MS}}(\mu) = w_{\mathcal{O}}^{\overline{\rm MS}}(\mu) \cdot Z_{\mathcal{O}}^{\rm RGI}$, again using the matching factor to the RGI value $w_{\mathcal{O}}^{\overline{\rm MS}}(\mu)$. Results of the RGI value and those in the $\overline{\rm MS}$ scheme at $\mu = 2$ GeV are

TABLE VII. Same as Table IV but for NF3p-b.

m_{ud}	$p^2_{\rm latt}$	C	$Z_q Z_m$	B_S	B_P	χ^2/dof
0.015	1.405	8.08(59)	1.464(13)	−2.30(94)	−0.99(55)	0.020
	1.851	6.92(49)	1.4009(98)	−1.57(63)	−0.57(35)	0.029
	2.279	5.97(42)	1.3527(78)	−1.04(50)	−0.34(29)	0.010
	2.690	5.30(37)	1.3239(68)	−0.76(41)	−0.19(22)	0.007
0.025	1.405	7.04(42)	1.4699(93)	−2.61(78)	−1.21(42)	0.012
	1.851	6.01(36)	1.4101(75)	−1.88(56)	−0.83(31)	0.004
	2.279	5.19(32)	1.3595(60)	−1.34(43)	−0.54(22)	0.003
	2.690	4.65(29)	1.3321(52)	−1.11(34)	−0.51(18)	0.005
0.035	1.405	7.14(50)	1.475(11)	−3.44(78)	−1.39(43)	0.146
	1.851	6.09(41)	1.4126(85)	−2.47(54)	−1.07(27)	0.087
	2.279	5.26(35)	1.3624(68)	−1.84(41)	−0.77(22)	0.095
	2.690	4.67(31)	1.3320(58)	−1.31(32)	−0.48(18)	0.059
0.050	1.405	8.93(56)	1.423(15)	−0.1(1.3)	0.03(55)	0.295
	1.851	7.59(47)	1.3755(99)	−0.09(84)	0.03(37)	0.325
	2.279	6.52(41)	1.3363(77)	−0.16(63)	−0.01(29)	0.200
	2.690	5.85(36)	1.3115(65)	−0.04(50)	0.02(22)	0.240
0.100	1.405	8.68(56)	1.468(16)	−1.7(1.2)	−0.61(60)	0.123
	1.851	7.34(48)	1.412(12)	−1.21(91)	−0.49(46)	0.113
	2.279	6.26(40)	1.3650(87)	−1.00(66)	−0.41(29)	0.072
	2.690	5.61(35)	1.3353(75)	−0.59(54)	−0.24(26)	0.104

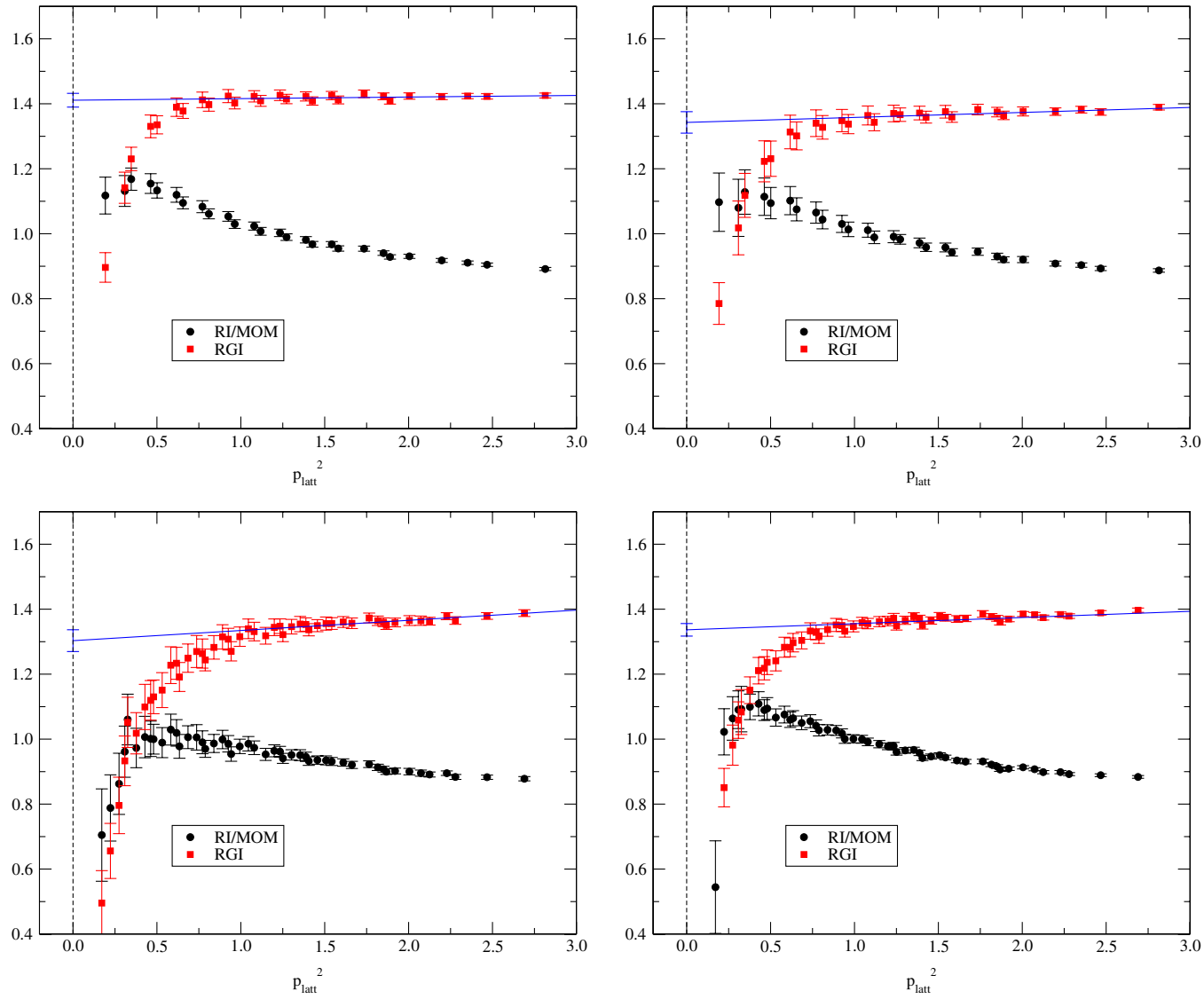

FIG. 11 (color online). Renormalization factors for the quark mass Z_m in the RI/MOM scheme (circles) and their RGI values (squares) as functions of $p^2_{\rm latt}$ for NF2ϵ (upper-left panel), NF2p (upper-right panel), NF3p-a (lower-left panel), and NF3p-b (lower-right panel). Results of the linear extrapolation to the $(p_{\rm latt})^2 \to 0$ limit of $Z_m^{\rm RGI}$ are shown as well. For NF2p, NF3p-a, and NF3p-b, data with a fixed sea quark mass $m_{\rm sea}(m_{ud}) = 0.015$ are plotted as an example.

listed in Table VIII for $\mathcal{O} = m$ and S with the four-loop level matching, and in Table IX for $\mathcal{O} = T$ with the three-loop level matching.

For the NF2p ensembles the renormalization factors at finite sea quark masses are extrapolated to the limit of $m_{\rm sea} = 0$ as a linear function of $2m^2_{\rm sea}$. For the $2+1$-flavor data, we combine NF3p-a and NF3p-b to quote the final result in the chiral limit of all three flavors, assuming a sea quark mass dependence of the form $Z(1 + c^{(3)}(2m^2_{ud} + m^2_s))$. The extrapolation is shown in Figs. 13 and 14 for the NF2p (left panels) and NF3p-a/b (right panels) ensembles. Although we do not observe any systematic sea quark mass dependence, the data show larger fluctuations than the statistical errors at each sea quark mass for Z_m. As a result, the χ^2/dof for the combination of NF3p-a and NF3p-b is uncomfortably large (~ 2.6), as listed in Table VIII. This may indicate that the statistical error estimated at each sea quark mass is underestimated. This is also suggested from the size of the statistical error at a fixed sea quark mass, say $m_{\rm sea}$(or m_{ud}) $= 0.015$. Namely, the size of the error is comparable between NF2p and NF3p-a/b, though the statistics is more than a factor of 2 larger for NF2p. We use the jackknife method for the statistical analysis with a bin size of 50 HMC trajectories. Given the limited total length of trajectories (2500 for NF3p-a/b), the statistical error does not change much even if we increase the bin size to 100 trajectories. We do not investigate this point further, because the statistical

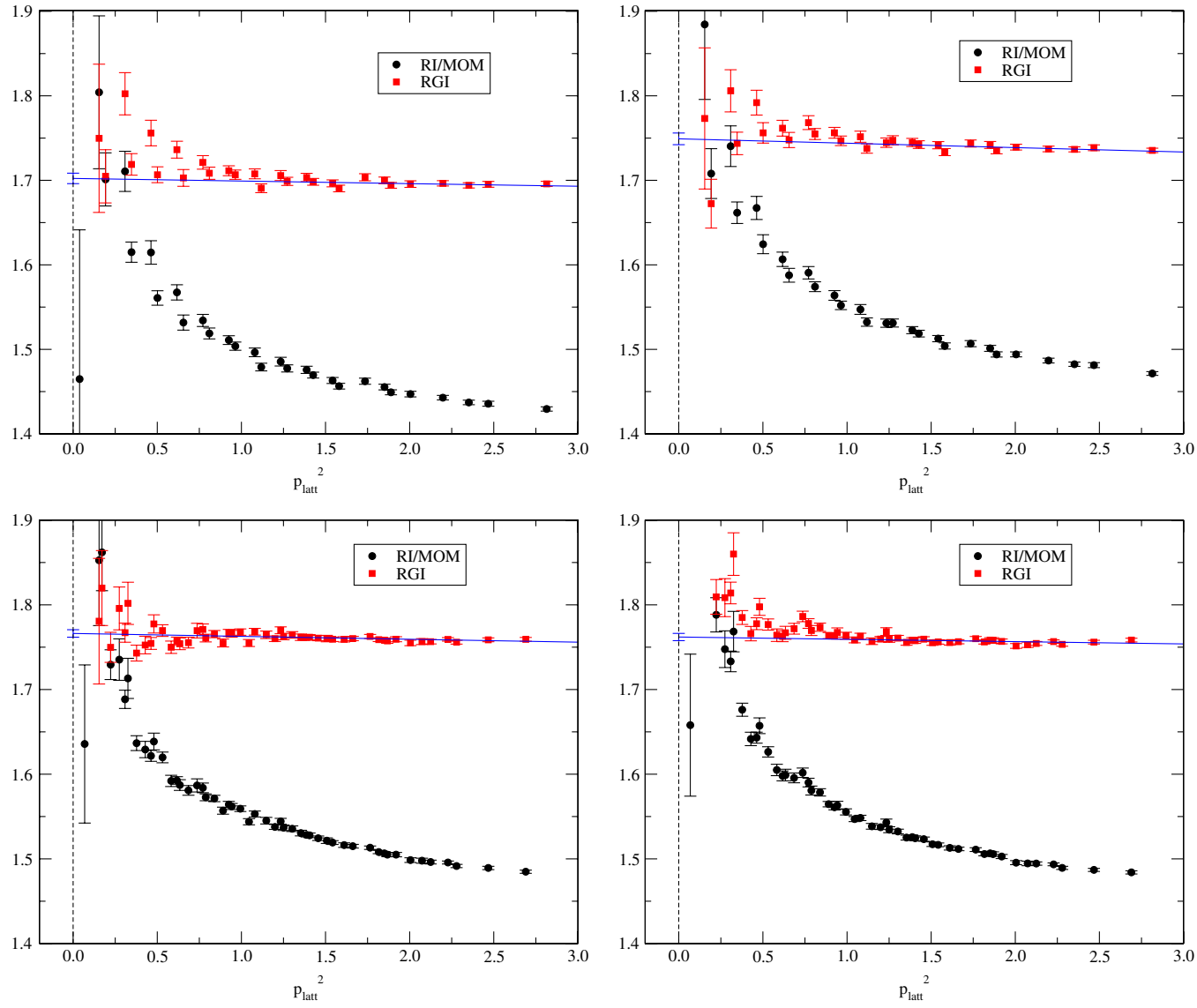

FIG. 12 (color online). Same as Fig. 11 but for the tensor current renormalization factor Z_T.

error does not give the dominant part of the error in the final results.

For the central values of the final results, we quote the result at $m_{\rm sea} = 0.002$ for NF2ϵ and that in the $m_{\rm sea} = 0$ limit for NF2p or in the $m_{ud} = m_s = 0$ limit for the combination of NF3p-a and NF3p-b. In Table VIII, the extrapolated values are listed in separate rows. The results for Z_m are

$$Z_m^{\overline{\rm MS}}(2\ {\rm GeV}) = \begin{cases} 0.824(14)(24)(^{+14}_{-00}) & \text{for } N_f = 2, \beta = 2.35 \\ 0.804(10)(25)(^{+00}_{-21}) & \text{for } N_f = 2, \beta = 2.30 \\ 0.806(12)(24)(^{+00}_{-11}) & \text{for } N_f = 2+1, \beta = 2.30. \end{cases} \tag{3.19}$$

The first error is statistical, and includes the small statistical errors in the extraction of $Z_A^{\rm WTI}$ and the lattice scale a^{-1}. The scale affects the determination of the matching point $\mu = 2$ GeV. On this error, we also take account of the ambiguity in removing the scale dependence of $Z_m^{\rm RGI}$ by comparing the results with different ranges of the linear fit. The systematic errors given in the second and third sets of parentheses are described in the following.

An important source of the systematic error is the truncation of the perturbative expansion in the matching between the RI/MOM and $\overline{\rm MS}$ schemes. It is given by a ratio of two matching factors to the RGI value, i.e. $w_m^{\rm RI/MOM}(\mu)$

TABLE VIII. Renormalization factors of the scalar operator and quark mass in the RGI and in the $\overline{\mathrm{MS}}$ schemes at $\mu = 2$ GeV. The results at each sea quark mass are listed, as well as those in the chiral limit of sea quarks.

$m_{\mathrm{sea}}(m_{ud})$		Z_S^{RGI}	Z_m^{RGI}	$Z_S^{\overline{\mathrm{MS}}}(2\ \mathrm{GeV})$	$Z_m^{\overline{\mathrm{MS}}}(2\ \mathrm{GeV})$
NF2ϵ	0.002	0.709(11)	1.411(21)	1.205(18)	0.830(12)
NF2p	0.015	0.743(18)	1.345(33)	1.263(30)	0.791(19)
	0.025	0.719(12)	1.390(24)	1.223(21)	0.818(14)
	0.035	0.764(20)	1.308(37)	1.298(35)	0.769(22)
	0.050	0.746(16)	1.339(29)	1.268(27)	0.788(17)
	0.070	0.726(14)	1.378(26)	1.234(23)	0.810(15)
	0.100	0.761(14)	1.313(26)	1.293(24)	0.772(15)
	0.000	0.7309(87)	1.366(16)	1.243(15)	0.8035(97)
	(χ^2/dof	1.15	1.15	1.15	1.15)
NF3p-a	0.015	0.766(19)	1.303(34)	1.296(32)	0.770(20)
	0.025	0.734(10)	1.362(20)	1.242(17)	0.805(12)
	0.035	0.721(17)	1.386(33)	1.221(29)	0.819(19)
	0.050	0.757(15)	1.320(27)	1.281(25)	0.780(16)
	0.080	0.765(17)	1.304(31)	1.296(29)	0.770(18)
NF3p-b	0.015	0.748(11)	1.337(19)	1.265(18)	0.790(11)
	0.025	0.7354(62)	1.359(12)	1.245(11)	0.8031(70)
	0.035	0.7311(87)	1.368(17)	1.238(15)	0.8078(98)
	0.050	0.774(13)	1.289(23)	1.310(22)	0.761(14)
	0.100	0.748(13)	1.336(25)	1.266(22)	0.789(15)
"Chiral limit":		0.7325(88)	1.364(16)	1.240(15)	0.8057(97)
	(χ^2/dof	1.61	1.64	1.61	1.64)

and $w_m^{\overline{\mathrm{MS}}}(\mu)$ in (A1). The perturbative expansion of these factors is given in (A2) and known to four-loop order. By setting $\mu = 2$ GeV, we may evaluate how it depends on the loop order. For $N_f = 2$, the ratio $w_m^{\overline{\mathrm{MS}}}(\mu)/w_m^{\mathrm{RI/MOM}}(\mu)$ becomes 1, 0.911, 0.863, and 0.835 when the perturbative expansion includes $O(\alpha_s^0)$, $O(\alpha_s^1)$, $O(\alpha_s^2)$, and $O(\alpha_s^3)$ terms, respectively. From this observation, we find that the perturbative expansion converges such that the additional correction is about 60% of the correction of the previous order. The same level of the correction is observed for the case of $N_f = 2 + 1$. We therefore assume that this convergence persists at the next unknown perturbative coefficient. The second error in (4.4) is estimated by taking the difference of the current best four-loop analysis and the second best three-loop analysis and multiplying by a factor 0.6.

The effect of SCSB may arise in two different ways. First, in the extraction of Z_q we used the axial-vector vertex function Λ_A, but if we used the vector vertex function Λ_V instead, the result would be slightly shifted, as given in the third set of parentheses. Note that this does not matter for NF2ϵ, because there is no significant difference between Λ_V and Λ_A in the ϵ regime. Second, one may expect some uncertainty in the process of subtraction of the power-divergent piece from $\langle \bar{q}q \rangle^{(N)}$. In Sec. III C, we demonstrate that the power-divergent term can be removed

TABLE IX. Same as Table VIII but for Z_T.

$m_{\mathrm{sea}}(m_{ud})$		Z_T^{RGI}	$Z_T^{\overline{\mathrm{MS}}}(2\ \mathrm{GeV})$
NF2ϵ	0.002	1.7023(62)	1.4689(53)
NF2p	0.015	1.7461(69)	1.5066(59)
	0.025	1.7418(63)	1.5030(54)
	0.035	1.7393(70)	1.5008(61)
	0.050	1.7470(72)	1.5075(62)
	0.070	1.7361(63)	1.4981(54)
	0.100	1.7330(64)	1.4953(55)
	0.000	1.7441(38)	1.5050(33)
	(χ^2/dof	0.24	0.24)
NF3p-a	0.015	1.7662(44)	1.5283(38)
	0.025	1.7663(50)	1.5284(43)
	0.035	1.7685(54)	1.5303(47)
	0.050	1.7591(38)	1.5222(33)
	0.080	1.7674(48)	1.5294(41)
NF3p-b	0.015	1.7620(43)	1.5247(37)
	0.025	1.7630(42)	1.5255(37)
	0.035	1.7637(42)	1.5261(36)
	0.050	1.7518(43)	1.5159(37)
	0.100	1.7640(56)	1.5264(48)
"Chiral limit":		1.7639(35)	1.5262(30)
	(χ^2/dof	1.18	1.18)

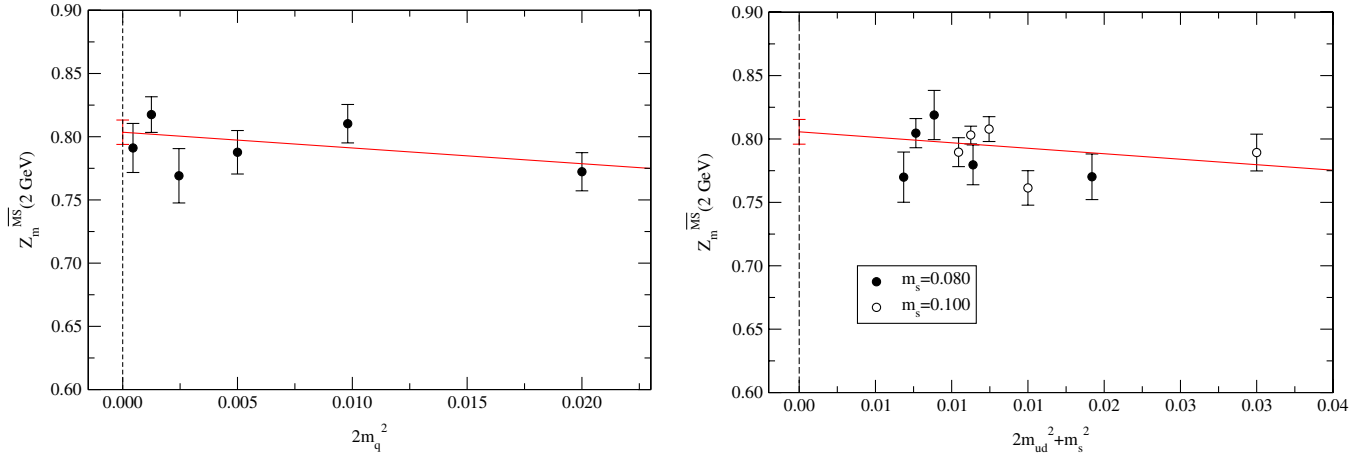

FIG. 13 (color online). Left panel: $Z_m^{\overline{\mathrm{MS}}}(2\ \mathrm{GeV})$ for NF2p as a function of $2m_{\mathrm{sea}}^2$. Right panel: Same value for NF3p-a and NF3p-b as a function of $2m_{ud}^2 + m_s^2$. Linear extrapolation to the $m_{\mathrm{sea}} = 0$ limit or the $m_{ud} = 0$ limit is shown as well.

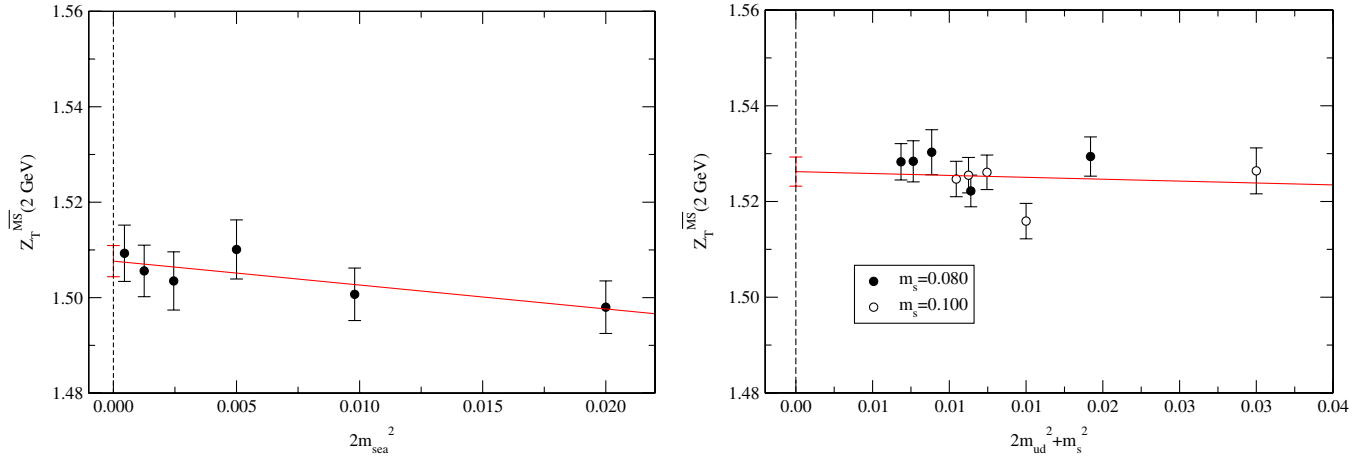

FIG. 14 (color online). Same as Fig. 13 but for $Z_T^{\overline{\mathrm{MS}}}(2\ \mathrm{GeV})$.

from $\langle\bar{q}q\rangle^{(N)}$ to obtain $\langle\bar{q}q\rangle^{(\mathrm{subt})}$ in an almost N-independent way. However, this does not guarantee that the results for $\langle\bar{q}q\rangle^{(\mathrm{subt})}$ are unchanged beyond the maximum value of N we studied. In fact, in the p regime, we find that $\Sigma \equiv \langle\bar{q}q\rangle^{(\mathrm{subt})}$ $(m_q = 0)$ obtained with various values of N slightly increases as a function of N. In the calculation based on chiral perturbation theory on the same ensembles [10,30], we find $\approx 10\%$ larger values of Σ than those from the eigenvalue decomposition for NF2p and NF3p-a/b. For NF2ϵ, the result of the calculation based on the chiral random matrix theory [11] is $\approx 10\%$ smaller. To estimate the effect of the truncation of eigenvalues, we repeat the same analysis by fixing the value of Σ to be 10% smaller (larger) than the original one for NF2ϵ (NF2p and NF3p-a/b). As a result, we find that the magnitude of a finite N effect is similar to the statistical errors for all cases. We quote the difference from the central value in the third error in (4.4). For NF2p and NF3p-a/b, we combine this error with the effect from the difference between Λ_A and Λ_V, which is in the same direction.

For completeness, we also present results for Z_T. Matching procedures are illustrated in Fig. 12. Table IX summarizes the RGI and the $\overline{\mathrm{MS}}$ values. The left and right panels in Fig. 14 show the linear extrapolation as a function of $2m_{\mathrm{sea}}^2$ (NF2p) and $2m_{ud}^2 + m_s^2$ (NF3p-a/b), respectively.

IV. CONCLUSION

We calculated the renormalization factors for the quark bilinear operators constructed from the overlap fermion formulation, based on the original idea of NPR proposed in [1]. The aim of this calculation is to provide the renormalization factors for a series of numerical studies being performed by the JLQCD and TWQCD Collaborations using dynamical overlap fermions. By virtue of the exact chiral symmetry of the overlap fermion, the analysis is

largely simplified compared to other nonchiral fermion formulations.

Through the simulation in the ϵ regime, we explicitly confirm that the vector and axial-vector vertex functions agree with each other when the effect of spontaneous chiral symmetry breaking is negligible. This may provide a clean way to calculate the renormalization factors through the NPR method, since the calculation does not suffer from the potential problems due to pion poles.

In the p regime, where spontaneous symmetry breaking effectively remains even on a finite volume lattice, we may precisely control the nonperturbative quark mass dependence of the quark propagator and vertex functions using the OPE analysis supplemented by the condensate explicitly constructed from the low-lying quark eigenmodes. The exact chiral symmetry of the overlap fermion plays an important role also in this analysis.

As the final result, we quote

$$Z_A = Z_V = \begin{cases} 1.3511(12) & \text{for } N_f = 2, \beta = 2.35 \\ 1.382\,22(82) & \text{for } N_f = 2, \beta = 2.30 \\ 1.393\,60(48) & \text{for } N_f = 2+1, \beta = 2.30, \end{cases} \tag{4.1}$$

$$Z_q^{\overline{\mathrm{MS}}}(2\ \mathrm{GeV}) = \begin{cases} 1.4799(50) & \text{for } N_f = 2, \beta = 2.35 \\ 1.5170(31) & \text{for } N_f = 2, \beta = 2.30 \\ 1.5296(31) & \text{for } N_f = 2+1, \beta = 2.30, \end{cases} \tag{4.2}$$

$$Z_T^{\overline{\mathrm{MS}}}(2\ \mathrm{GeV}) = \begin{cases} 1.4689(53) & \text{for } N_f = 2, \beta = 2.35 \\ 1.5050(33) & \text{for } N_f = 2, \beta = 2.30 \\ 1.5262(30) & \text{for } N_f = 2+1, \beta = 2.30, \end{cases} \tag{4.3}$$

and

$$Z_m^{\overline{\mathrm{MS}}}(2\ \mathrm{GeV}) = \begin{cases} 0.824(14)(24)(^{+14}_{-00}) & \text{for } N_f = 2, \beta = 2.35 \\ 0.804(10)(25)(^{+00}_{-21}) & \text{for } N_f = 2, \beta = 2.30 \\ 0.806(12)(24)(^{+00}_{-11}) & \text{for } N_f = 2+1, \beta = 2.30, \end{cases} \tag{4.4}$$

where the errors are statistical except for Z_m.

Our main results are those of the mass renormalization factor Z_m, which is an inverse of the scalar density renormalization factor Z_S. The result has already been used in the calculation of the chiral condensate in two-flavor QCD from the Dirac operator spectrum [11,12] and from the topological susceptibility [14]. It has also been used in our calculation of the up and down quark mass through the analysis of the pion mass and decay constant [15]. Extension of these works to the $2+1$-flavor case is in progress.

By using the value of $Z_m^{\overline{\mathrm{MS}}}$ we quoted in this article, we are planning to determine the up and down quark mass m_{ud} and the strange quark mass m_s from the analysis of the meson masses m_π^2 and m_K^2 and the decay constants f_π and f_K in the $N_f = 2+1$ dynamical simulation. A preliminary results from this project was reported in [16].

ACKNOWLEDGMENTS

Numerical simulations are performed on Hitachi SR11000 and the IBM System Blue Gene Solution at the High Energy Accelerator Research Organization (KEK) under the support of its Large Scale Simulation Program (No. 07-16 and No. 08-05). We thank Professor C. Sachrajda for informative discussions. H. F. is supported in part by the Global COE Program "Quest for Fundamental Principles in the Universe" of Nagoya University provided by Japan Society for the Promotion of Science (G07). This work is supported in part by the Grant-in-Aid of the Ministry of Education (No. 18740167, No. 18840045, No. 19540286, No. 19740121, No. 19740160, No. 20025010, No. 20039005, No. 20740156, No. 20105002, No. 20105005, No. 21674002) and the National Science Council of Taiwan (No. NSC96-2112-M-002-020-MY3) and NTU-CQSE (No. 97R0066-65 and No. 97R0066-69).

APPENDIX: PERTURBATIVE MATCHING

In this appendix, we present the details of our matching procedure.

The matching of an operator $\mathcal{O}$ between the $\overline{\mathrm{MS}}$ scheme and the RI/MOM scheme is written as

$$\mathcal{O}^{\overline{\mathrm{MS}}}(\mu) = \frac{w_{\mathcal{O}}^{\overline{\mathrm{MS}}}(\mu)}{w_{\mathcal{O}}^{\mathrm{RI/MOM}}(\mu_0)} \mathcal{O}^{\mathrm{RI/MOM}}(\mu_0), \tag{A1}$$

where the conversion factor $w_{\mathcal{O}}^{X}(\mu)$ from a given scheme X to the so-called RGI value is written as

$$w_{\mathcal{O}}^{X}(\mu) = \alpha_S(\mu)^{\bar{\gamma}_0}\Bigg[1 + (\bar{\gamma}_1 - \bar{\beta}_1\bar{\gamma}_0)\frac{\alpha_S(\mu)}{4\pi} + \frac{1}{2}((\bar{\gamma}_1 - \bar{\beta}_1\bar{\gamma}_0)^2 + \bar{\gamma}_2 + \bar{\beta}_1^2\bar{\gamma}_0 - \bar{\beta}_1\bar{\gamma}_1 - \bar{\beta}_2\bar{\gamma}_0)\left(\frac{\alpha_S(\mu)}{4\pi}\right)^2 + \left(\frac{1}{6}(\bar{\gamma}_1 - \bar{\beta}_1\bar{\gamma}_0)^3 + \frac{1}{2}(\bar{\gamma}_1 - \bar{\beta}_1\bar{\gamma}_0)(\bar{\gamma}_2 + \bar{\beta}_1^2\bar{\gamma}_0 - \bar{\beta}_1\bar{\gamma}_1 - \bar{\beta}_2\bar{\gamma}_0) + \frac{1}{3}(\bar{\gamma}_3 - \bar{\beta}_1^3\bar{\gamma}_0 + 2\bar{\beta}_1\bar{\beta}_2\bar{\gamma}_0 - \bar{\beta}_3\bar{\gamma}_0 + \bar{\beta}_1^2\bar{\gamma}_1 - \bar{\beta}_2\bar{\gamma}_1 - \bar{\beta}_1\bar{\gamma}_2)\right)\left(\frac{\alpha_S(\mu)}{4\pi}\right)^3\Bigg]_X, \tag{A2}$$

to the four-loop order in terms of the strong coupling constant $\alpha_S(\mu)$. (For the coupling constant, we always use the $\overline{\text{MS}}$ scheme.) The coefficients $\bar{\beta}_i$ and $\bar{\gamma}_i$ are given in terms of the coefficients of the β function $\beta(\alpha_S)$ and the anomalous dimension $\gamma_{\mathcal{O}}(\alpha_S)$,

$$\beta = -\beta_0\frac{\alpha_S^2}{4\pi} - \beta_1\frac{\alpha_S^3}{(4\pi)^2} - \beta_2\frac{\alpha_S^4}{(4\pi)^3} - \beta_3\frac{\alpha_S^5}{(4\pi)^4} - \cdots, \tag{A3}$$

$$\gamma_{\mathcal{O}} = -\gamma_{\mathcal{O}}^{(0)}\frac{\alpha_S}{4\pi} - \gamma_{\mathcal{O}}^{(1)}\left(\frac{\alpha_S}{4\pi}\right)^2 - \gamma_{\mathcal{O}}^{(2)}\left(\frac{\alpha_S}{4\pi}\right)^3 - \gamma_{\mathcal{O}}^{(3)}\left(\frac{\alpha_S}{4\pi}\right)^4 - \cdots, \tag{A4}$$

as $\bar{\beta}_i = \beta_i/\beta_0$ and $\bar{\gamma}_i = \gamma_{\mathcal{O}}^{(i)}/\beta_0$.

The β function is specified by

$$\beta_0 = 11 - \tfrac{2}{3}N_f, \tag{A5}$$

$$\beta_1 = 102 - \frac{38}{3}N_f, \tag{A6}$$

$$\beta_2 = \frac{2857}{2} - \frac{5033}{18}N_f + \frac{325}{54}N_f^2, \tag{A7}$$

$$\beta_3 = \frac{149\,753}{6} + 3564\zeta_3 - \left(\frac{1\,078\,361}{162} + \frac{6508}{27}\zeta_3\right)N_f + \left(\frac{50\,065}{162} + \frac{6472}{81}\zeta_3\right)N_f^2 + \frac{1093}{729}N_f^3, \tag{A8}$$

with $\zeta_3 = 1.202\,056\,9$. The running coupling constant is then obtained as

$$\alpha_S(\mu) = \frac{4\pi}{\beta_0\ln\mu^2/\Lambda^2}\Bigg[1 - \frac{\beta_1}{\beta_0^2}\frac{\ln(\ln\mu^2/\Lambda^2)}{\ln\mu^2/\Lambda^2} + \frac{\beta_1^2}{\beta_0^4(\ln\mu^2/\Lambda^2)^2}\left((\ln\ln\mu^2/\Lambda^2)^2 - \ln(\ln\mu^2/\Lambda^2) + \frac{\beta_2\beta_0}{\beta_1^2} - 1\right) - \frac{\beta_1^3}{\beta_0^6(\ln\mu^2/\Lambda^2)^3}\left((\ln\ln\mu^2/\Lambda^2)^3 - \frac{5}{2}(\ln\ln\mu^2/\Lambda^2)^2 - \left(2 - \frac{3\beta_0\beta_2}{\beta_1^2}\right)\ln\ln\mu^2/\Lambda^2 + \frac{1}{2} - \frac{\beta_0^2\beta_3}{2\beta_1^3}\right)\Bigg]. \tag{A9}$$

In our work, we chose $\Lambda = 245$ MeV for both two- and 2 + 1-flavor analysis.

The renormalization of the scalar bilinear operator $\mathcal{O} = S = \bar{q}q$ is an inverse of the mass renormalization. The anomalous dimension thus has a relation $\gamma_m = -\gamma_S$. At the lowest order, $\gamma_m^{(0)} = 4$ for any scheme. Higher order coefficients are calculated in [31] to the four-loop order in the RI/MOM scheme,

$$\gamma_m^{(1)} = 126 - \frac{52}{9}N_f, \tag{A10}$$

$$\gamma_m^{(2)} = \frac{20\,911}{3} - \frac{3344}{3}\zeta_3 + \left(-\frac{18\,386}{27} + \frac{128}{9}\zeta_3\right)N_f + \frac{928}{81}N_f^2, \tag{A11}$$

$$\gamma_m^{(3)} = \frac{300\,665\,987}{648} - \frac{15\,000\,871}{108}\zeta_3 + \frac{6160}{3}\zeta_5 + \left(-\frac{7\,535\,473}{108} + \frac{627\,127}{54}\zeta_3 + \frac{4160}{3}\zeta_5\right)N_f + \left(\frac{670\,948}{243} - \frac{6416}{27}\zeta_3\right)N_f^2 - \frac{18\,832}{729}N_f^3, \tag{A12}$$

and in the $\overline{\text{MS}}$ scheme,

$$\gamma_m^{(1)} = \frac{202}{3} - \frac{20}{9}N_f, \tag{A13}$$

$$\gamma_m^{(2)} = 1249 - \left(\frac{2216}{27} + \frac{160}{3}\zeta_3\right)N_f - \frac{140}{81}N_f^2, \tag{A14}$$

$$\gamma_m^{(3)} = \frac{4\,603\,055}{162} + \frac{135\,680}{27}\zeta_3 - 8800\zeta_5 - \left(\frac{91\,723}{27} + \frac{34\,192}{9}\zeta_3 - 880\zeta_4 - \frac{18\,400}{9}\zeta_5\right)N_f + \left(\frac{5242}{243} + \frac{800}{9}\zeta_3 - \frac{160}{3}\zeta_4\right)N_f^2 - \left(\frac{332}{243} - \frac{64}{27}\zeta_3\right)N_f^3, \quad \text{(A15)}$$

where $\zeta_3 = 1.202\,057$, $\zeta_4 = \pi^4/90$, and $\zeta_5 = 1.036\,928$.

For the quark field renormalization ($\mathcal{O} = q$), the lowest order coefficient vanishes in the Landau gauge for any scheme. The higher order coefficients for the RI/MOM scheme are [31]

$$\gamma_q^{(1)} = \frac{67}{3} - \frac{4}{3}N_f, \quad \text{(A16)}$$

$$\gamma_q^{(2)} = \frac{43\,477}{36} - \frac{607}{2}\zeta_3 - \left(\frac{3674}{27} - 16\zeta_3\right)N_f + \frac{80}{27}N_f^2, \quad \text{(A17)}$$

$$\gamma_q^{(3)} = \frac{54\,714\,743}{648} - \frac{7\,004\,309}{162}\zeta_3 + \frac{15\,846\,715}{1296}\zeta_5 - \left(\frac{4\,659\,455}{324} - \frac{637\,413}{162}\zeta_3 + 830\zeta_5\right)N_f + \left(\frac{166\,269}{243} - 64\zeta_3\right)N_f^2 - \frac{688}{81}N_f^3, \quad \text{(A18)}$$

while the $\overline{\text{MS}}$ coefficients are

$$\gamma_q^{(1)} = \frac{67}{3} - \frac{4}{3}N_f, \quad \text{(A19)}$$

$$\gamma_q^{(2)} = \frac{20\,729}{36} - \frac{79}{2}\zeta_3 - \frac{550}{9}N_f + \frac{20}{27}N_f^2, \quad \text{(A20)}$$

$$\gamma_q^{(3)} = \frac{2\,109\,389}{162} - \frac{565\,939}{324}\zeta_3 + \frac{2607}{4}\zeta_4 - \frac{761\,525}{1296}\zeta_5 - \left(\frac{162\,103}{81} + \frac{2291}{27}\zeta_3 + \frac{79}{2}\zeta_4 + \frac{160}{3}\zeta_5\right)N_f + \left(\frac{3853}{81} + \frac{160}{9}\zeta_3\right)N_f^2 + \frac{140}{243}N_f^3. \quad \text{(A21)}$$

Coefficients for the tensor current $\mathcal{O} = T = \bar{q}\sigma_{\mu\nu}q$ are known to three-loop order [3,32]. Besides the common value $\gamma_T^{(0)} = 4/3$, higher order coefficients for the RI/MOM scheme are

$$\gamma_T^{(1)} = \frac{362}{9} - \frac{52}{27}N_f, \quad \text{(A22)}$$

$$\gamma_T^{(2)} = \frac{159\,607}{81} - \frac{13\,072}{27}\zeta_3 + \left(-\frac{17\,426}{81} + \frac{256}{27}\zeta_3\right)N_f + \frac{928}{243}N_f^2, \quad \text{(A23)}$$

and those for the $\overline{\text{MS}}$ scheme are

$$\gamma_T^{(1)} = \frac{362}{9} - \frac{52}{27}N_f, \quad \text{(A24)}$$

$$\gamma_T^{(2)} = \frac{52\,555}{81} - \frac{928}{27}\zeta_3 - \left(\frac{5240}{81} + \frac{160}{9}\zeta_3\right)N_f - \frac{4}{9}N_f^2. \quad \text{(A25)}$$

[1] G. Martinelli, C. Pittori, C. T. Sachrajda, M. Testa, and A. Vladikas, Nucl. Phys. **B445**, 81 (1995).
[2] T. Blum *et al.*, Phys. Rev. D **66**, 014504 (2002).
[3] Y. Aoki *et al.*, Phys. Rev. D **78**, 054510 (2008).
[4] T. A. DeGrand and Z.-f. Liu, Phys. Rev. D **72**, 054508 (2005).
[5] J. B. Zhang *et al.*, Phys. Rev. D **72**, 114509 (2005).
[6] D. Galletly *et al.*, Phys. Rev. D **75**, 073015 (2007).
[7] S. Aoki *et al.* (JLQCD Collaboration), Phys. Rev. D **78**, 014508 (2008).
[8] S. Hashimoto *et al.* (JLQCD Collaboration), Proc. Sci., LAT2007 (2007) 101 [arXiv:0710.2730].
[9] H. Matsufuru *et al.* (JLQCD and TWQCD Collaborations), Proc. Sci., LAT2008 (2008) 077.
[10] H. Fukaya *et al.*, Phys. Rev. D **76**, 054503 (2007).
[11] H. Fukaya *et al.* (JLQCD Collaboration), Phys. Rev. Lett. **98**, 172001 (2007).
[12] H. Fukaya *et al.* (JLQCD Collaboration), Phys. Rev. D **77**, 074503 (2008).
[13] S. Aoki *et al.* (JLQCD and TWQCD Collaborations), Phys. Lett. B **665**, 294 (2008).
[14] T.-W. Chiu, T.-H. Hsieh, and P.-K. Tseng (TWQCD Collaboration), Phys. Lett. B **671**, 135 (2009).
[15] J. Noaki *et al.* (JLQCD and TWQCD Collaborations), Phys. Rev. Lett. **101**, 202004 (2008).
[16] J. Noaki *et al.*, Proc. Sci., LAT2008 (2008) 107 [arXiv:0810.1360].
[17] H. Neuberger, Phys. Lett. B **417**, 141 (1998).
[18] H. Neuberger, Phys. Lett. B **427**, 353 (1998).
[19] S. Duane, A. D. Kennedy, B. J. Pendleton, and D. Roweth, Phys. Lett. B **195**, 216 (1987).
[20] H. Fukaya *et al.* (JLQCD Collaboration), Phys. Rev. D **74**, 094505 (2006).
[21] Y. Iwasaki, Report No. UTHEP-118, 1983.

[22] S. Aoki, H. Fukaya, S. Hashimoto, and T. Onogi, Phys. Rev. D **76**, 054508 (2007).
[23] E. Shintani *et al.* (JLQCD Collaboration), Phys. Rev. D **79**, 074510 (2009).
[24] C. Sturm *et al.*, Phys. Rev. D **80**, 014501 (2009).
[25] L. Giusti and A. Vladikas, Phys. Lett. B **488**, 303 (2000).
[26] H. D. Politzer, Nucl. Phys. **B117**, 397 (1976).
[27] J. Gasser and H. Leutwyler, Ann. Phys. (N.Y.) **158**, 142 (1984).
[28] P. H. Damgaard and H. Fukaya, J. High Energy Phys. 01 (2009) 052.
[29] S. Aoki *et al.* (JLQCD and TWQCD Collaborations), Phys. Rev. D **80**, 034508 (2009).
[30] H. Fukaya *et al.* (JLQCD Collaboration), arXiv: 0911.5555.
[31] K. G. Chetyrkin and A. Retey, Nucl. Phys. **B583**, 3 (2000).
[32] J. A. Gracey, Nucl. Phys. **B662**, 247 (2003).